Particle-Based Porous Material Development for Capillary Condensation Applications

by

Shichao Jiao

Bachelor of Engineering, Chongqing University, 2014

M.S., Columbia University, 2016

Submitted to the Graduate Faculty of the

Swanson School of Engineering in partial fulfillment

of the requirements for the degree of

Doctor of Philosophy

University of Pittsburgh

2023

UNIVERSITY OF PITTSBURGH

SWANSON SCHOOL OF ENGINEERING

This dissertation was presented

by

Shichao Jiao

It was defended on

January 19, 2023

and approved by

Sachin Velankar, PhD, Professor, Department of Chemical and Petroleum Engineering

Susan Fullerton, PhD, Professor, Department of Chemical and Petroleum Engineering

Andrew Bunger, PhD, Professor, Department of Surgery, Department Civil & Environmental Engineering, Department of Chemical and Petroleum Engineering

Dissertation Director: Joseph J. McCarthy, PhD, Professor, Department of Chemical and Petroleum Engineering

Particle-Based Porous Material Development for Capillary Condensation Applications

Shichao Jiao, PhD

University of Pittsburgh, 2023

The 21st-century challenge of securing an abundant fresh water supply has led to a growing trend of harnessing atmospheric water[1]. Water scavenging approaches have primarily leveraged daily heating/cooling cycles[2–4], using techniques such as mimicking desert beetles[5] to capture early-morning fog using synthetic netting[6] or biomimetic materials[7], and exploiting solar energy more[8] to enhance water release from metal-organic framework (MOF) based sorbent materials[8,9]. We describe a facile way to control capillary condensation via confined geometric structures, using this behavior to create novel composite materials for water scavenging. By employing a particle self-assembly technique, we fabricate porous materials with well-defined, controllable pore sizes. Controlling the scale and number of confined spaces allows direct control of capillary condensation behavior. We predict capillary condensation induced by exposing these materials to a humid environment, with water uptake isotherms qualitatively agreeing with predictions across all samples.

Our novel water scavenging composite is created by forming a hierarchically ordered porous material from a suitable hydrogel and embedding closely packed particles within its surfaces. This configuration amplifies native material performance and realizes synergy between the capture and storage of scavenged water. The composite can capture moisture at a significantly lower relative humidity than native materials alone. Although challenges like insufficient mechanical strength and the need for scalable methods remain, compared to MOFs, which

represent the current state of the art, our material outperforms them by a factor of 1.25~2.5 in terms of water harvesting capability. This approach has potential for a cheap, low-energy clean water source and could be adapted for various condensible vapor reclamation applications.

Finally, we computationally examine the phenomenon of "lubrication collapse" that underpins the particle self-assembly approach. By studying a range of forcing patterns and strengths for confined particle-laden flows, we identify cases where the one-particle Stokes number allows particles to cross fluid streamlines and collide, while the two-particle Stokes number ensures viscous interactions significantly reduce relative particle velocities. Manipulating flow parameters in this manner helps devise criteria for generating flows that lead to local enrichment or complete dispersion of included particles.

Table of Contents

List of Tables

List of Figures

Preface

The path to completing this dissertation has been both enlightening and challenging, granting me an in-depth understanding of my area of study and the chance to contribute to the existing knowledge base. The work presented herein is the result of countless hours spent on research, experimentation, analysis, and writing. I am deeply appreciative of the support, guidance, and encouragement I have received from various individuals throughout this endeavor.

I would like to take this opportunity to express my sincere gratitude to Dr. Joseph McCarthy, my advisor, for his steadfast support, guidance, and mentorship throughout this journey. I am also thankful to my committee members, Dr. Sachin Velankar, Dr. Susan Fullerton, and Dr. Andrew Bunger, for their valuable feedback and suggestions that have substantially improved the quality of this work.

Additionally, I would like to acknowledge my fellow researchers, colleagues, and friends who have provided valuable insights, encouragement, and camaraderie during this process. Finally, I am deeply grateful to my girlfriend for her unwavering love and support throughout my academic journey.

I dedicate this dissertation to my parents, whose never-ending support and love have been with me since the day I was born.

1.0 Introduction

As the size of the system decreases to the nanoscale, the surface effect becomes very important. It is well known that a confined fluid's phase behavior differs from that in bulk[10,11]. In nanoscale confinement, phase behavior is influenced by liquid-wall/pore interactions. Capillary condensation is the process of multilayer adsorption of the vapor molecules into liquid phase on the surfaces of confined structures, which has been realized for decades[12]. The importance of capillary condensation is getting increasing attention with the non-negligible physical effect such as hysteresis[13], capillary adhesion[14], lubrication, and friction[15–17].

The capillary condensation of water, among all different liquids, attracts the most attention. Even though the capillary condensation of water is commonly seen in nature and has a significant impact on our daily lives, many unknowns are still yet to be investigated. The trapping of molecules in confinement and the formation and growth of primary water clusters in the nanostructure has not been fully understood under different environments. The key to understanding capillary condensation and employing the knowledge in a wide range of applications needs both theoretical and experimental studies. One of the emerging applications utilizing capillary condensation of water is atmospheric water capture. Ensuring a sufficient supply of fresh water is one of the most significant challenges of the 21st century[18]. For decades researchers from across the globe have examined a variety of techniques for generating clean water[19] from desalination[20] to disinfection/ decontamination[21,22]. More recently, a growing trend aims to harness the abundant supply of freshwater that is available within the atmosphere[1]. While a variety of different materials have been developed for atmospheric water capture, the core idea

behind this is the same: a confined space needs to be created to allow capillary condensation. Despite the great efforts in developing those different materials, which showed great promise and good performance of water retention, the applications of those materials are greatly limited by the difficulty of recovery of the water due to high energy consumption and the low adaptability of the materials in a harsh environment and poor stabilities[23].

The main object of the presented work is to explore a novel idea of creating a composite material in a simple but effective way of realizing the scavenging of water from the atmosphere. Here, we use self-organization of closely-packed particle crystalline structure to create controllable proximities between particles for the capillary condensation to occur. Furthermore, hydrophilic hydrogel is used as a reservoir for the captured water, allowing an easy release of water. The principle of capillary condensation is validated via water uptake isotherms among different particle sizes. Moreover, a thermodynamic analysis is performed to describe the observed results from the composite. Furthermore, an exploration of a better way of realization of particle self-assembly in suspension is conducted using a computational method.

The dissertation is organized as follows. Chapter 2.0 reviews the relevant background materials, including the basic information about porous materials, capillary condensation, and different self-assembly techniques, as well as a discussion of the simulation methodology. Chapter 3.0 validates the nature of capillary condensation by creating various porous materials using the particle self-assembly technique. Chapter 4.0 presents the preparation of the novel composite for atmospheric water scavenging. The experimental results and the characterizations of the composite are presented. The theoretical prediction is developed based on the Flory-Huggins absorption theory and kelvin equation that ties the absorption to the capillary condensation in confinement.

Chapter 5.0 explores the experimental conditions for the scaled-up particle self-assembly via the simulation method. Finally, Chapter 6.0 discusses our conclusions and the outlook of this work.

2.0 Background

The study of porous materials, especially the adsorption in porous materials, has been going on for a century[24]. Nevertheless, many problems remain unsolved, and new problems arise as new materials are developed, and environmental conditions change. Water shortage[25] has become a constant issue humans have been facing for decades. There has been a significant amount of work done for clean water generation[19,26,27]. Meanwhile, a significant amount of fresh water, over three quadrillion gallons, is stored in the atmosphere[28]. Thus, there has been an increasing effort on one's ability to capture (or scavenge) water directly from the atmosphere[5,6,8,9,29–34]. This chapter will cover the basics of atmospheric molecule adsorption – capillary condensation, common porous materials, and the simulation method we used in the thesis.

2.1 Capillary Condensation

In nanoporous media with pore diameters less than 100 nm, the molecular size and the mean free path cannot be ignored[10,35,36]. Due to the confinement, intermolecular forces are more significant, and phase behavior is no longer just a function of fluid-fluid interactions but also a fluid-wall interaction[37].

Capillary condensation, which is the process of multilayer adsorption of the vapor molecules into liquid phase on the surfaces of the confined structures, has been realized for decades[12]. It routinely occurs in granular and porous materials, can strongly alter properties such

as hysteresis[13], capillary adhesion[14], lubrication, friction, and corrosion[17,38–40], and is essential in many industrial processes with granular or porous media like pharmaceuticals and semiconductors[41].

Capillary condensation of water, among all different liquids, attracts the most attention since water adsorption is essential for many applications requiring capture and, sometimes, the release of water[29]. For example, microporous oxides such as zeolites are commonly used as electric dehumidifiers[42], atmospheric water capture devices have been developed by different groups hoping to provide extra fresh water in certain areas[43], and water capture and release devices were investigated in the design of adsorption-driven heat exchangers[44–48].

Even though the capillary condensation of water is commonly seen in nature and has a significant impact on our daily lives, many unknowns are still yet to be investigated. The trapping of molecules in confinement and the formation and growth of primary water clusters in the nanostructure has not been fully understood. Here we will first introduce the basic Kelvin equation and advanced models derived from the Kelvin equation. Then we will discuss the current studies focused on the sub-10-nm scale. And last, we will discuss the current effort on atmospheric water capture.

2.1.1 The Kelvin Equation

Before the capillary condensation occurs, the capillary pressure is the only form of interfacial pressure and exists as the pressure difference between the adsorbed layers and the vapor phase[38,49,50], which is defined by the Young-Laplace equation,

$$P_{cap} = \frac{2\gamma}{r_P} cos\theta \qquad \textbf{Eq(2.1)}$$

Where γ is the surface tension, r_P is the radius of the pore, and θ is the contact angle of the meniscus with the pore wall. When the equilibrium shifts, adsorbed films converge upon each other, and the center of the pore will be filled with the liquid phase, which is separated from the vapor phase by a meniscus[50]. And new equilibrium has been reached between the bulk vapor and the liquid phase in the pore. This phenomenon, capillary condensation, was quantitatively described by Bocquet et al. using the Kelvin equation[13],

$$\frac{\gamma_{lv}}{r} = \rho_l k_B T \ln\left(\frac{P^v}{P_{Sat}}\right) \qquad \textbf{Eq(2.2)}$$

Where P^v is the vapor pressure, P_{Sat} is the saturated vapor pressure when the surface is flat, γ_{lv} is the liquid/vapor surface tension, k_B is the Boltzmann constant, T is the temperature, ρ_l is the density of the liquid phase, and *r* is the radius of the meniscus.

The Kelvin equation has been used extensively in the past few decades for both experiments and simulations to describe capillary condensation[51,52]. It is often used to predict the occurrence of capillary condensation in different situations[38,53,54]. More recently, some groups have attempted to extend the Kelvin equation to describe extreme situations such as sub-10-nm pores more accurately. These efforts typically include the effect of the meniscus on the surface tension[55] and adjustments of pore radius according to the shape or the thickness of the adsorbed phase[56,57].

2.1.2 Advanced Models

In order to account for all the assumptions the Kelvin equation made, various versions of advanced models were developed. In this section, we are going to introduce major advanced models briefly.

2.1.2.1 Density Functional Theory

Density functional theory (DFT) relies on minimizing the grand potential energy, which accounts for all the thermodynamic energies throughout the system, to achieve the most steady state, which can be used for the investigation of hysteresis[10,41,50,58]. DFT also accounts for pore geometries and fluid-pore interactions. Simulations using the DFT method have gained popularity for accurately estimating pore size distribution[41,50]. However, the DFT method has shown some inaccuracies attributed to the oversimplifications of the pore wall surface roughness and the improper treatments of pore-fluid potentials[59].

2.1.2.2 Molecular Simulation

Similar to the DFT method, molecular simulation offers a microscopic evaluation of capillary condensation[41]. It was carried out primarily due to the lack of experimental data for adsorbents of different wettability and pore geometry. Grand canonical Monte Carlo simulation (GCMC) and Molecular Dynamic (MD) are the most commonly used molecular simulation methods[60–64]. Because molecular simulation accounts for interactions of every single molecule and atom, it can describe more complicated molecular structures and provide a more invasive investigation of the underlying mechanisms of capillary condensation. However, limited by

computational power, an extensive amount of simulation time is required to perform a realistic result. Otherwise, the oversimplifications of functions and algorithms will lead to inaccurate results[62,65].

2.1.3 Capillary Condensation in Sub-10-Nm Scale

Even though the Kelvin equation is still the most commonly used model for simple estimations and numerical calculations[50,66–78], there were some uncertainties in capillary condensation predictions in the sub-10-nm pores[75–77]. Nevertheless, with the advancement of both computational and experimental methods, more and more studies indicated the validity of the Kelvin equation in sub-10-nm pores[69–72]. For example, Zhong et al.[71]conducted experiments using a nanofluidic device confirming the validity of the Kelvin equation in 8-nm channels, Factorovich et al.[79] studied the evaporation pressure of water droplets with a diameter of as small as 1.2 nm using GCMD method and claimed the accuracy of the prediction from the Kelvin equation, Seongsoo Kim[80] using AFM method showed that Kelvin equation is valid down to approximately 0.5 nm.

2.1.4 Atmospheric Water Capture

One of the significant applications of capillary condensation is atmospheric water capture. In the face of rapidly increasing consumption, accelerated environmental degradation, and more significant impacts from climate change, we need new ways to face the challenge of increasing demand for freshwater.[18] While desalination has attracted much attention in recent decades, its

location-based limitations necessitate distribution infrastructure, which imposes a significant upfront capital cost[27,81,82]. Meanwhile, over three quadrillion gallons of fresh water are in the atmosphere[28]. There have been some methods in the literature for recovering water from the atmosphere, including atmospheric water generators and various absorbent materials such as hydrogels, oxides, zeolites, MOFs, and other materials[6,8,9,29–33]. To date, such water scavenging approaches have primarily leveraged daily heating/cooling cycles to overcome the energetic cost of condensation[2–4]. Some mimic the behavior of the desert beetle[5] to capture early-morning fog using, for example, synthetic netting[6] or other biomimetic materials[7]. These approaches capitalize on the temperature decrease at specific times of the day, which causes the relative humidity to rise to 100%. Consequently, water molecules in the air condense and are collected by the modified surfaces. However, these methods and materials necessitate saturated water vapor in the atmosphere, significantly constraining their practicality. In contrast, other researchers have focused on exploring water harvesting from unsaturated atmospheres[8,9]. For instance, another technique exploits solar energy more[8] directly in order to enhance the release of water captured within a metal-organic framework (MOF) based sorbent material[8,9]. However, the advances in the applications of those devices are hindered by their high energy consumption for water recovery [5,34].

2.2 Ordered Porous Material

The study of capillary condensation advances with the development of knowledge and techniques of porous materials. The study of capillary condensation has changed dramatically with the discovery of highly ordered materials such as MCM-41[83] and SBA-15[84] in the 1990s. This section will introduce typical ordered porous materials such as zeolites, MOFs, and particle-based porous materials.

2.2.1 Zeolites

The traditional zeolites are microporous, crystalline aluminosilicate materials commonly used as adsorbents and catalysts[85]. The general formula of zeolites is.

$$A_x^n(SiO_2)(AlO_2)_x \cdot yH_2O$$

Where A_x^n is either a metal ion or H^+. The basic units of zeolites are AlO_4 and SiO_4 tetrahedra. And most of the zeolites are formed by linking the corner oxygen atoms of the unit tetrahedra. As of 2018, there are more than 200 different zeolites[86]. Nevertheless, despite many studies attempting to address this issue, their micropores impose limitations on mass transport[87].

In recent years, several highly ordered mesoporous materials, such as MCM-41[83] and SBA-15[84] have been discovered. These materials sustain the characteristics of zeolites, such as acidity, crystallinity, porosity, and stability[87] , and have a characteristic hexagonal arrangement of uniform mesopores, as shown in Figure 2.1.

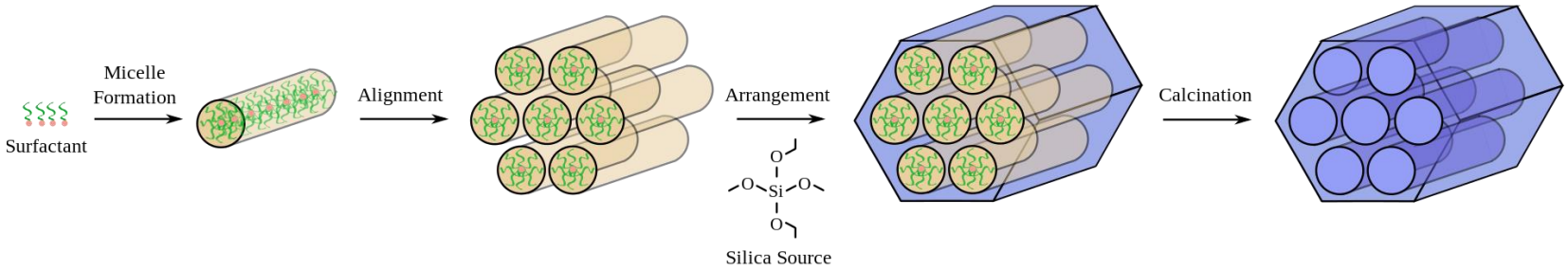

Figure 2.1 Synthesis pathway of MCM-41 (after dissertation Markus Reichinger, Ruhr-Universität Bochum, 2007)

2.2.2 MOFs

Metal-organic framework (MOF) is a more recently discovered ordered porous material, crystalline material with metal ions or clusters and organic ligands containing potential voids[88]. It is constructed from inorganic clusters linked by organic molecules to form crystalline framework structures[89]. It has gained tremendous popularity due to its great tunability of chemical and structural properties[90]. The excellent porosity and stability exhibited by some of the MOFs make them great candidates for gas adsorption and storage[91]. Consequently, MOF is also one of the proposed materials as sorbents for atmospheric water capturing[92]. The metal ions of MOFs are connected to the organic structures, which have strong affinity for polar molecules such as water molecules. Water molecules are strongly attracted to the cavity inside the unit, which creates great difficulty for the desorption process.

2.2.3 Particle Self-Assembly/Particle-Based Structures

In 1959, Prof. Feynman proposed the idea of manipulating chemical structures one atom at a time[93]. While the manipulation at the atomic level is still in the early stage, the control of colloidal particles with a similar idea but a few orders of magnitude larger has become a very popular topic. Among all the techniques of forming ordered porous materials, colloidal crystal templating is one of the most promising techniques that are still under development[94,95]. Colloidal particles, typically monodispersed and spherical, are considered as building blocks to form, via

self-assembly, crystals[96]. These crystals are either directly used as porous materials by themselves, with additional treatment to overcome the brittleness of the close-packed lattice, or can be used as templates to form porous materials via their interstices[97–99]. In general, colloidal particles brought great interest in a variety of areas, including photonic/ plasmonic devices, nano-electronics, energy-storage, drug/gene delivery, hierarchically structured catalysts etc.[100]

To serve the purpose of colloidal particle assembly, scientists have been studying the size, shape, surface properties, and interactions of different colloidal particles[96,101,102]. This bottom-up approach provides great convenience of creating nano to macro structures as well as brings some unique properties. However, the self-assembly of particles is not easy since, according to thermodynamics, our nature tends to be more disordered. For colloidal particles to self-assemble, they first need to be the right shape which is mostly spherical. Secondly, the proper force needs to be in place for self-assembly to happen. For nano, micro, meso, and macro particles, which are all widely dealt with in engineering applications, the driving forces of self-assembly vary with the radius of particles. For particles small enough, the driving force of self-assembly could be interactions between atoms and molecules, such as Van der Waals or electrostatic force. Particularly in fluid media, which is often the case, the Brownian motion of fluid molecules is often the driving force leading to self-assembly[97,103]. For larger particles such as meso and especially macro particles, some mechanical forces due to the contact between particles are also playing important roles, such as friction[104]. In this case, the natural thermal effects are no longer able to overcome the kinetic barriers, which produce the need for external agitation force to maintain the mobility and structural adjustability of the colloidal system in order to induce large

particle self-assembly, just like what Brownian motion does to the small colloidal particle system[105,106]

2.2.4 Adsorptive Characterization

The theory developed by Brunauer, Emmet, and Teller (BET)[107] is the most commonly used adsorptive method to characterize the specific surface area of a material. It has been the primary tool to assess the surface properties of a porous material since its first publication. One has to note that despite the popularity of the BET method, it comes with some underlying assumptions[108]. Firstly, the material is assumed to have a homogeneous surface. Secondly, from the second layer and above, molecules can be adsorbed before the complete filling of the previous layers. Thirdly, there is no lateral interaction between the molecules in the same layer. And the BET formula can be described as,

$$\mathrm{q} = q_m \left(\frac{C\left(\frac{p}{p_0}\right)}{\left(1 - \frac{p}{p_0} + C\left(\frac{p}{p_0}\right)\right)\left(1 - \frac{p}{p_0}\right)} \right) \qquad \textbf{Eq(2.3)}$$

Where q is the adsorbed amount, q_m is the BET monolayer capacity, p_0 is the saturated vapor pressure, $\frac{p}{p_0}$ is the relative pressure, and C is the dimensionless BET parameter, which is approximated by[109]:

$$\mathrm{C} \approx \exp\left(\frac{E_1 - E_2}{RT}\right) \qquad \textbf{Eq(2.4)}$$

Where E_1 and E_2 is the molar adsorption energy for the first layer and second and above layers.

On the other hand, the pore size distribution is calculated using a method developed by Barrett, Joyner, and Halenda (BJH)[56]. The BJH method characterizes pore size distribution independent of the external area using the Kelvin model of pore filling. Thus, the BET and BJH methods are often coupled in porous material characterizations, where the BET method provides the surface area information, and the BJH method provides additional information on pore size, volume, and distribution.

2.3 Simulation Method

A theoretical approach can provide a straightforward solution to a simple case. However, a computational method provides a much more accurate and effective solution when it comes to complex cases. Computational fluid dynamics (CFD) is a set of numerical methods used to predict the motion of fluids. With the improvement of computing power and the development of the simulation method, CFD has become one of the primary methods for the simulation of complex fluid dynamics[110]. Lattice Boltzmann Method (LBM) is the CFD method used in this dissertation.

Similarly, the Discrete Element Method (DEM) is a simulation technique that computes the mechanical interactions between a pair of particles[111]. In the last part of this work, we use LBM coupled with DEM as a computational approach to evaluate the particle-particle interactions in a fluidic environment. In this section, we introduce the basics of LBM and DEM.

2.3.1 Lattice Boltzmann Method

The Lattice Boltzmann Method (LBM) was developed from the Lattice Gas Cell Automata models (LGCA)[112], which uses a lattice in which every cell stores a Boolean particle or flag. Each lattice contains a direction vector e_i indicating the moving direction. The LGCA method consists of two steps: streaming and collision. In the streaming step, each molecule is copied along the direction vector to the next lattice; the collision step happens when two molecules move into a single cell from the opposite direction, they collide and get redirected by a Boolean operation. LBM overcomes the disadvantages of the LGCA method, such as the large noise-signal ratio, by replacing the Boolean flag with the distribution function f_i, which describes the proportion of material at that node with momentum in the direction i. The distribution function is the primary variable of the LBM, which is critical for determining the velocity and density of the fluid domain.

The LBM equation is given by:

$$f_i(\boldsymbol{x} + \boldsymbol{c_i}\Delta \mathrm{t}, \mathrm{t} + \Delta \mathrm{t}) - f_i(\boldsymbol{x} + t) = \Omega_i(f(\boldsymbol{x}, t)) \qquad \textbf{Eq(2.5)}$$

Where f_i is the distribution function, $\Delta \mathrm{t}$ is the explicit time step, and $\boldsymbol{c_i}$ is the lattice speed. Ω_i is the collision operator, which determines the rate of change of the distribution function after the collision step.

2.3.2 Discrete Element Method

The particle interactions are captured using the Discrete Element Method (DEM). This method integrates Newton's translational and rotational equations to determine the motion of the

particles. The particle forces can include frictional, gravitational, and adhesive forces, among others.

$$m_i \frac{d^2}{dt^2} \boldsymbol{r}_i = \boldsymbol{f}_{ii} + m_i \boldsymbol{g} \qquad \textbf{Eq(2.6)}$$

$$\boldsymbol{I}_i \frac{d}{dt} \boldsymbol{w}_i = \boldsymbol{t}_i \qquad \textbf{Eq(2.7)}$$

Where m_i is the mass of the particle, $\boldsymbol{r}_i$ is the position, $\boldsymbol{g}$ is the gravity vector, $\boldsymbol{I}_i$ is the momen of inertia of the particle, $\boldsymbol{w}_i$ is the angular velocity, and $\boldsymbol{f}_{ii}$ is the total forces including the normal and tangential forces between particles as well as the coupling forces for momentum transport between particles and the fluid.

In this work, DEM is used to capture the particle-particle interaction and is coupled to LBM in order to take into consideration the momentum transport between the fluid and particles.

3.0 A Facile Way of Controlling Capillary Condensation: Particle-Based Crystal

To demonstrate a facile method to control capillary condensation via the design of confined geometric structures, we use a particle self-assembly technique to fabricate porous materials with well-defined pore sizes. Four groups of silica particles were synthesized using the modified Stober method, and these groups of particles were then arranged in closely-packed structures. Quantitative predictions of capillary condensation were made based on the Kelvin equation and an approximation of the geometric structures of our closely-packed samples. The water uptake isotherms qualitatively agree with predictions across all samples, despite the fact that the geometry of some of the confined spaces corresponds to distances smaller than 10 nm. This fabrication method shows great potential for the creation of devices that allow facile control of capillary condensation in relevant applications such as vapor capture and humidity control.

3.1 Introduction

It is well known that a confined fluid's phase behavior differs from that of the bulk[10,41]. In particular, under nanoscale confinement, the observed phase behavior is influenced by liquid-wall/pore interactions. Capillary condensation is a resulting phenomenon that significantly impacts many fields relevant to water[8,113], air[114], and energy[115–118]. While a continuum-level understanding has been well-established, the initiation of nucleation and the propagation of capillary condensation in nanostructured materials is not fully understood. In recent years, both theoretical

and experimental studies have been aimed at establishing a better understanding of capillary condensation, especially down to the sub-10-nm scale[17,80,90].

The foundation of continuum-level theoretical studies of phase behavior under confinement is the century-old Kelvin equation[50] derived from the Young-Laplace equation[38]. The Kelvin equation has been used extensively since its development to describe capillary condensation[61,71,80,119–121], primarily at scales where the continuum approximation is well accepted. On the other hand, there has been some recent debate regarding the validity of the Kelvin equation down to the sub-10-nm level[75–77]. Thus, in the past two decades, researchers have examined alternative ways to describe this phenomenon, including the development of models that consider the thermodynamic energies throughout all phases using such techniques as density functional theory[10,11,50,62], grand canonical Monte Carlo simulation[63,64] , and Molecular Dynamics[49,122].

At the same time, experimental studies have aimed to validate these theories and models as well as to provide new insight into existing theories. Needless to say, directly investigating the nucleation site at the single molecular level is challenging. Thus, the majority of the prior experimental studies involve interpreting the absorptive data from standard porous media, including hydrophilic solids such as silica gels, zeolites, and some classes of metal-organic frameworks[17,90]. More recently, technological advances have enabled researchers to probe capillary condensation at the sub-10-nm level via a number of techniques. For example, measurement of a "critical" tip-surface distance can be made using atomic force microscopy (AFM) to identify when capillary condensation/nucleation occurs. In order to accomplish this measurement, the sharp AFM tip is slowly made to approach a surface. When a sudden drop of the tip’s amplitude is realized, it is inferred that the spontaneous formation of a water meniscus has occurred, and the "critical" distance is realized (and interpreted to represent the distance

necessary to induce nucleation at a particular relative humidity). By varying the relative humidity in the environment of this apparatus, one can obtain a series of experimental values of the critical distance corresponding to different relative humidities[80]. While this technique is quite powerful, it is difficult to experimentally maintain both ultra-low (i.e., 2%) and ultra-precise humidities for the time required to perform the AFM experiments. This may explain why, for very low humidities, the measured critical distance is found to be significantly different from the theoretical values that are predicted by the Kelvin equation. In contrast, several competing experimental efforts have appeared to support the validity of the Kelvin equation at the sub-10 nm scale[69–72]. For example, one group used a nanofluidic device[71] to help understand capillary condensation at the nanoscale. They directly measured condensation initiation and dynamics within 8 nm deep silicon nanochannels. Their results suggest that the initiation of capillary condensation in the sub-10-nm scale agrees closely with the Kelvin equation. Similarly, a group recently studied condensation using atomic-scale capillaries created by two-dimensional crystals, forming capillary geometries as small as four angstroms. The observations in that work suggested that the Kelvin equation can quantitatively describe capillary condensation at scales even smaller than a nanometer[121].

As a complement to these detailed experimental studies, this paper demonstrates a facile method to manipulate capillary condensation over a range of humidities by placing particles onto surfaces in order to create confined geometric structures. Specifically, highly controllable and ordered porous structures are created using a simple particle self-assembling technique. Using these surfaces, we are able to demonstrate the ability to control the capillary condensation behavior by changing the size distribution of the particles that are deposited on the surfaces. Theoretical predictions based on the Kelvin equation show agreement with adsorption experiments that not only demonstrate that this methodology is effective at condensation control, but these results also

lend support to the applicability of the Kelvin equation at scales below that of 10-nm. We believe that further exploration of this method could lead to exciting applications relevant to capillary condensation, such as vapor capture, humidity control, and more.

3.2 Experimental Section

In this section, we describe the materials and method to synthesize silica particles and the preparation of the multilayer structure. The characterization methods and equipment settings will also be introduced.

3.2.1 Materials and Characterization.

Tetraethyl orthosilicate (TEOS), ethanol (C_2H_5OH), and ammonium hydroxide solution (NH_4OH) were obtained from Sigma-Aldrich. The silicon wafers used were obtained from University Wafer Inc.

Where applicable, the particle size distribution was characterized by Zetasizer Nano S. This was accomplished as follows. The particle suspension was diluted prior to the measurement. 1 ml of the suspension solution was added to the disposable cuvette, which was then inserted into the instrument. At least three independent runs were taken for each sample, and the count rate and correlation factor were checked to ensure the quality of the measurements.

The structure of the particle layers on the silicon wafer was characterized using the scanning electron microscope (SEM) Zeiss Sigma 500 VP Analytical FE-SEM. The operation

voltage varied from 1 kV to 10 kV depending on the particle size and the layer thickness. The morphological structure of the sample was also characterized by an atomic force microscope (AFM) using a Bruker Nano Multimode.

3.2.2 Preparation of Silica Particles and the Multilayer Structure.

Silica particles with different size distributions were synthesized using the modified Stober method under room temperature conditions[123] The appropriate amount of ethanol, deionized water, and ammonia solution was mixed in a 20 ml transparent glass vial. Then a certain quantity of tetraethyl orthosilicate (TEOS) solution was added according to the desired ratio (appropriate to the target particle size) in the mixed solution. The vial was vigorously shaken for 30 seconds, and then the reaction was allowed to proceed at ambient temperature for 12 hours. The solution can be used as-is or diluted for further analysis and experiments.

Particles of 4 different sizes are successfully synthesized using the modified Stober method (see Figure 3.1 for the relevant size distributions). All the particles prepared are stable, and the size distribution is narrow. Furthermore, the polydispersity is similar across all the experiments. Several factors contribute to polydispersity. Specifically, under certain conditions the initial generation of new primary particles exceeds the consumption of reagent used for the growth of existing particles. Also, the growth and aggregation of particles initiated at different stages can also lead to polydispersity[124]

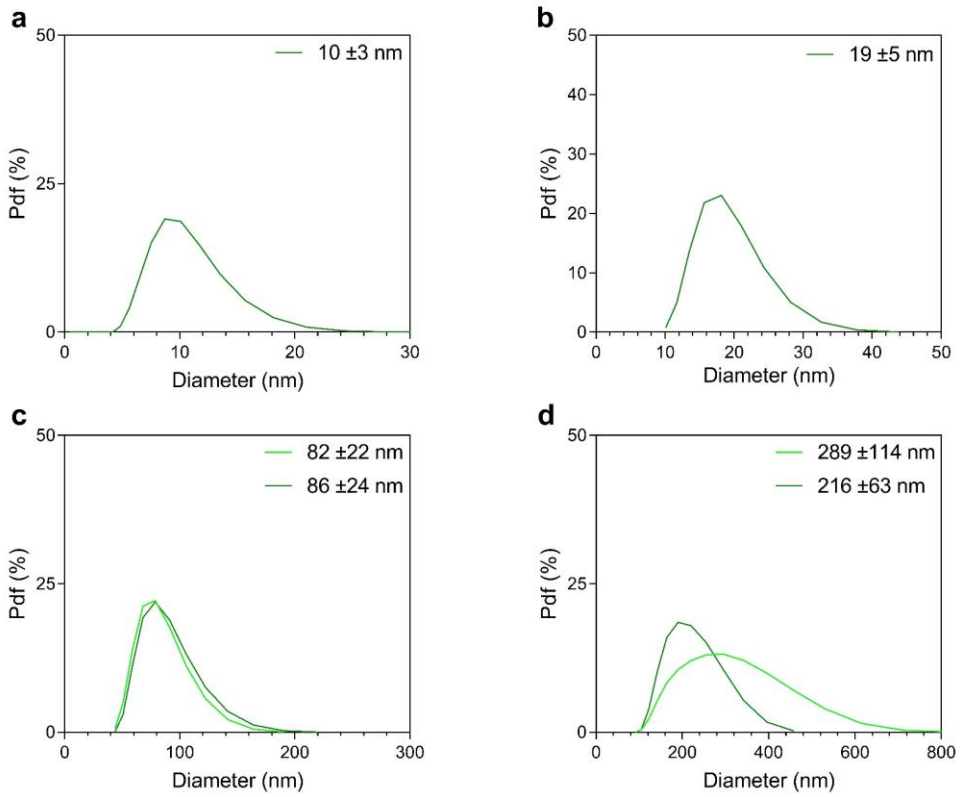

Figure 3.1 Particle size distributions of synthesized particles obtained using the Zetasizer: (a)10 nm, (b) 19 nm, (c) 82 nm and 86 nm, (d) 216 nm and 289 nm

After synthesis, the particle suspension was prepared for the evaporation self-assembly process by dilution with ethanol at a ratio of 1:4. The diluted suspension was then deposited onto the pre-cut clean silicon wafer surface. Depending on the experimental conditions, a heating plate or vacuum chamber may be used to speed up the evaporation process.

In the results quoted here, the self-assembled particle bed is created through the evaporation of solvent (i.e., ethanol in this case) that results in capillary forces arising between particles as the shrinking liquid volume forms inter-particle liquid bridges[125]. Figure 3.2 shows an AFM image of 35 nm particles deposited on a silicon wafer as described. The image shows that the spherical particles are agglomerated together, forming a multilayer structure. Figure 3.3 shows an SEM image of the 200 nm particle sample's deposition results. It can be seen that even for the largest particles used in our experiments, a closely-packed structure is achieved via the fast evaporation method. Moreover, Figure 3.3.b shows that the particles tend to aggregate with others of similar sizes and particles with smaller sizes tend to accumulate near the edge of the particle flocks. One can also notice defects in the multilayer structures due to the bubble formation inherent in the fast evaporation process. Since the defects are much larger in relative terms to the particles, the resulting pore spaces do not contribute significantly to the availability of condensation sites; thus, we note that the anticipated impact of these defects on the results quoted elsewhere in this paper is minimal.

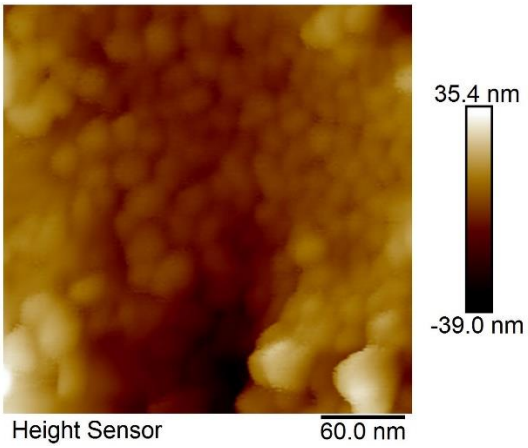

Figure 3.2 The atomic force microscopy image of a closely-packed multilayer of 35 nm particles deposited on a glass slide

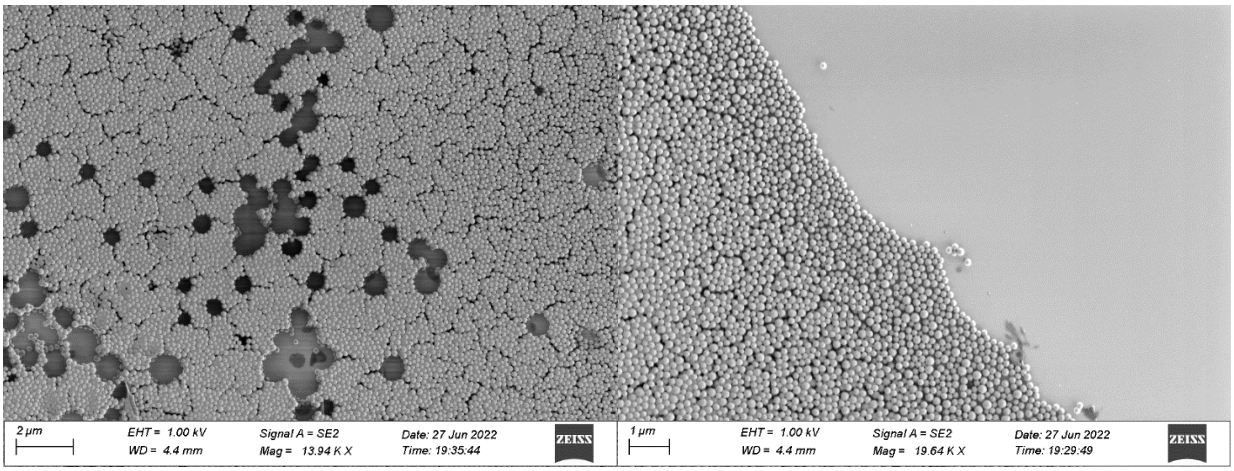

Figure 3.3 The scanning electron microscopy images of the 200 nm particles at the center (left) and the edge (right)

3.2.3 Adsorption Experiment

The multilayer particle beds are then tested under a series of different relative humidities (RH). Relative humidity control was realized by bubbling dry air through a temperature-controlled water bath which is held at varying temperatures to achieve different saturation humidities. After bubbling through the water bath, the humidified air is fed directly to a glove box. For the water-uptake measurements, particle samples are first dried under a vacuum inside an opened airtight bag for 24 hours. During this time, the humidity chamber is also in operation to ensure that it reaches the desired relative humidity prior to testing. After this period, the (still opened) airtight bags containing particle samples are transferred into the RH-controlled chamber and allowed to accumulate condensate. After waiting a sufficient time for the sample weight to stabilize (typically an additional 24 hours), the bags are sealed, and measurements of mass gain are made using a Mettler Toledo MS105DU balance.

3.3 Results and Discussion

In an effort to characterize the pore spaces between self-assembled particle layers, we have evaluated three different close-packed structures: Body-centered cubic (BCC), face-centered cubic (FCC), and hexagonal close-packed (HCP). Based on the approximation that the particles have a narrow size distribution, we assume them to be monodispersed within each cubic unit. Additionally, we assume that each single cubic unit cell within these packed structures can be used to inform the local values of the pore size distribution, as shown in Figure 3.4.. Ultimately, these

assumptions allow us to calculate a representative inter-particle pore size distribution from the measured particle size distributions of the samples such that we may infer theoretical water uptake values. It is important to note that the pore size distributions do not have a sharp cut-off because we explicitly account for the polydispersity of each particle and utilize the aforementioned assumptions to translate this polydispersity into pore size variation across the whole sample. One can see that the pore size distribution shifts slightly with different packing structures, but that the particle size sets the order of magnitude of each slate of pore distributions. For simplicity of calculation, the critical pore sizes were estimated based on the maximum curvature radius between the adjoining particles in each unit-cell structure and approximating each inter-particle pore as a perfect sphere with the requisite radius of curvature of the pore (See the complete calculation of the maximum curvature in Appendix B). While one notes that, in reality, the edges of the pore contain very sharp geometries, (eventually leading to a contact point between particles), the approach taken here allow simply theoretical predictions that represent a reasonable (but systemically larger value for) the critical humidity for the onset of capillary condensation within the particle systems. Moreover, the magnitude of this system approximation error increases as the particle size (and concomitantly the pore size) increases.

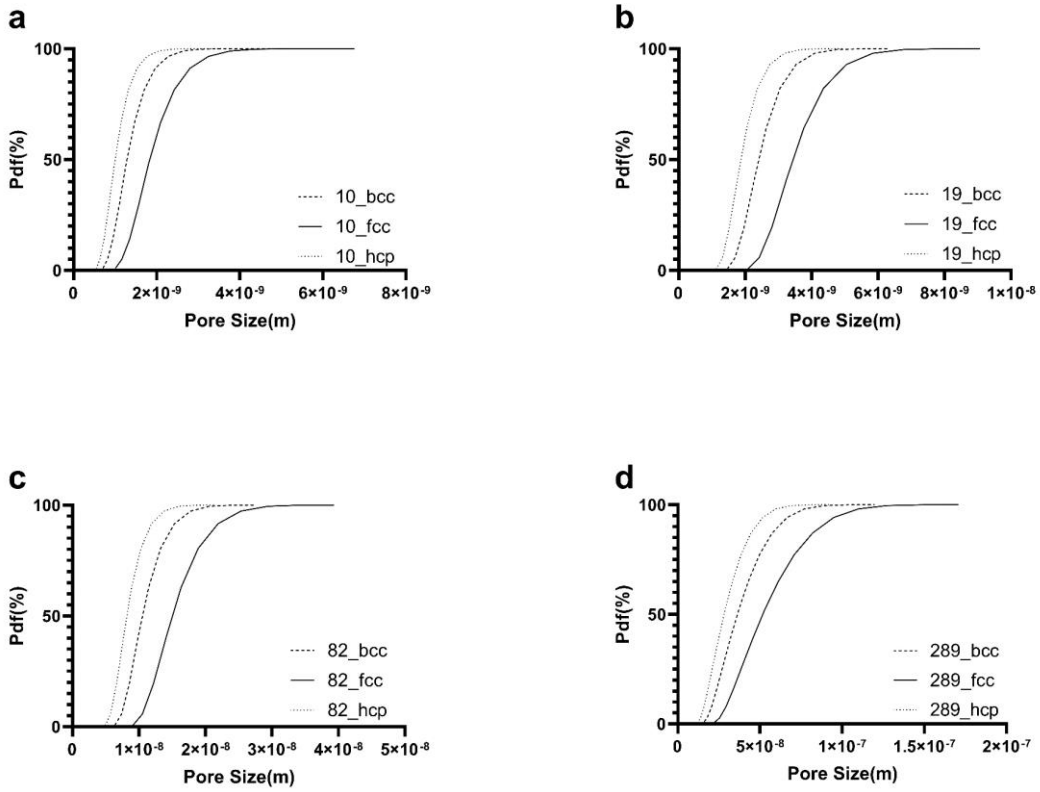

Figure 3.4 The estimated pore size distribution for different particle sizes: (a) 10 nm, (b) 19 nm, (c) 82 nm, (d) 289 nm.

As discussed in the previous chapter, the theoretical predictions of capillary condensation in our closely-packed structures are calculated based on the Kelvin equation (Eq(4.3)) and informed by measurements (and modeling) of the structure of our samples. The Kelvin equation is derived from the Laplace equation, which expresses the pressure difference across the curved surfaces of a liquid. According to the thermodynamic relations, the Kelvin equation leads to a relationship between the relative pressure (relative humidity in the water vapor case) and the principal radius of the curved surface.

Based on the Kelvin equation, the saturation vapor pressure will be depressed in the vicinity of the concave surfaces. Thus, for these geometries the relative humidity required for water vapor to condense is lower than that observed near a flat surface. That is, there will be a critical relative humidity value – which is lower than the 100% – that corresponds directly to the radius of the pores, and when the relative humidity is equal to or greater than this critical value the pore be filled with condensed water. Since, in reality, the inter-particle pore is not spherical, but instead has tight spacing at the edges of the pores, the requisite relative humidity for condensation will be lower than predicted in these areas (and the process of filling will initiate in these areas of smallest curvature); however, given that the bulk of the pore volume can be well-characterized by our approximations, the relative humidity that is associated with each specific pore size is indicative of the point at which the bulk of the water uptake is observed.

Using this approach, and based on the calculated pore size distribution of each sample (obtained from combining the unit cell analysis with the particle size distribution), we are able to predict the capillary condensation process from 0% relative humidity to 100% relative humidity for each of our experimental samples. The black and gray lines in Figure 3.5 show the theoretical water uptake predictions calculated based on the FCC, BCC packing, and HCP packing scenarios

(the solid line represents the FCC structure, the dashed line represents the BCC structure, and the dotted line represents the HCP structure). For comparison, the ability of the particle samples to induce capillary condensation is measured under different relative humidity using the previously-described humidity-controlled glove box. For each sample, the measurements are taken under different relative humidities ranging from 15% to 95%. For each measurement, the sample is allowed to reach equilibrium over a one-day exposure. Furthermore, the samples are thoroughly dried under vacuum between steps to ensure no residue affects the results. The masses of all tested samples are measured pre- and post-exposure (with samples sealed in an airtight bag for transport between the humidity chamber and scale). The absorptive performance is quantified based on the mass of water absorbed relative to the mass of the silica particles on the wafer.

We should note that a control wafer sample with no silica particles is also tested under both 50% and 90% RH. This control experiment resulted in no measurable water uptake, thus we can interpret all water uptake observed in Figure 3.5 to be the result of capillary condensation specifically within the pore spaces that are created by the presence of the closely-packed silica particles. In Figure 3.5 the water uptake results for samples with different particle size distributions are shown as the green triangles in each separate plot. It can be seen that, despite the difference in sizes, almost all samples ultimately achieved the same level of water retention, around 40% ~ 50%, near 100% relative humidity (due to essentially the same void fraction being observed for each sample). Thus, when all the pores are filled, the total mass of the water relative to the mass of the particles is similar in each case. Due to the narrow size distribution, the water uptake values increase dramatically over a relatively short range of relative humidity, especially for the samples comprised of very small particles. Again, here we emphasize that in the ideal situation (i.e., with a matrix formed by monodisperse particles), the water absorption will be a step change. In Figure

3.5a, we show an example of an ideal sample with 10 nm monodisperse particles in both BCC (thick dashed line) and FCC (thick solid line) packing. With an increase in the mean diameter of particles, the onset of water uptake requires a higher relative humidity. Also, the water uptake increases more slowly for larger particles due to the broader particle size distributions (and the more considerable discrepancy between the sharp point contacts and the, as-defined, "critical" pore sizes).

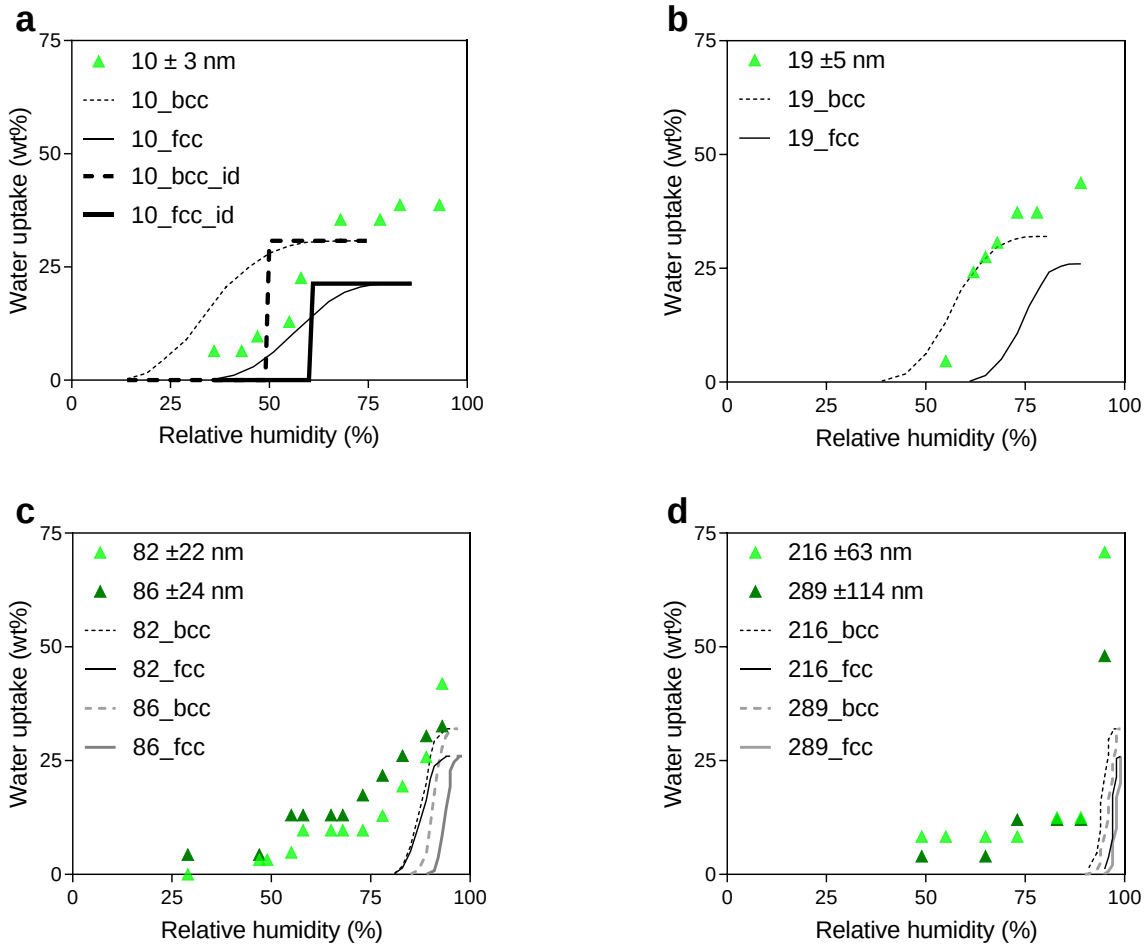

Figure 3.5 The theoretical and experimental values of water uptake for samples with different-size particles. The black and gray lines show the theoretical water uptake predictions calculated based on the FCC, BCC packing, and HCP packing scenarios (the solid line represents the FCC structure, the dashed line represents the BCC structure, and the dotted line represents the HCP structure). Water uptake results for samples with different particle size distributions are shown as the green triangles. An example of an ideal sample with 10 nm monodisperse particles in both BCC (thick dashed line) and FCC (thick solid line) packing is shown in (a).

In Figure 3.5, for samples with smaller particle sizes, the experimental observations coincide well with the theoretical predictions. Notice that for larger particles, noticeable differences are evident between the experimental water uptake curves relative to those based on the theoretical predictions. In order to rationalize this, we emphasize that the overall packing structure of our sample is not exactly represented by any of the three structures we used in the theory to predict water uptake. Also, despite our approximation, the pores created within these closely-packed structures are not spherical; instead, the pores can be tetrahedral, octahedral, or even more complicated, depending on the relative positioning of the adjoining particles. Thus, the more sharply-curved portions of the pores will start nucleating water below the theoretical "critical" relative humidity due to the existence of the more minor curvatures. In other words, as expected, we always overestimate the relative humidity at which the onset of capillary condensation occurs. Moreover, for samples that include bigger particles (100s of nm), the discrepancy between the sharp contact points between particles and the pore sizes estimated from the inter-particle distances can differ by up to an order of magnitude. As such, the water uptake before the critical relative humidity is considerably more apparent in these cases. Nevertheless, it is heartening that we predict, and observe, a plateauing of the water uptake at intermediate humidities for the samples containing small particles. However, we do not either predict or observe such a plateau for the larger-particle samples (other than the consistent evidence of a lower uptake value plateau that is observed near 50% relative humidity and which we attribute to condensation exclusively at particle contact spots). Finally, one can also notice that the ultimate water uptake near 100% relative humidity is always higher than the theoretical value. We anticipate that this is due to the filling of the aforementioned "large pore" defects created from our evaporative self-assembly technique, which are ultimately filled at very high relative humidity and lead to more

water uptake near 100% relative humidity. This discrepancy is particularly evident for the 200 nm sample, as may be anticipated from the image included in Figure 3.3 (left).

3.4 Conclusion

In summary, a closely-packed particle matrix with controllable pore sizes is fabricated using a simple evaporative particle self-assembly method. This porous material with controllable sizes is tested for water uptake isotherms and compared against a simplified theoretical model. The experimental results show substantial agreement with our theoretical predictions of capillary condensation, particularly for systems comprised of very small particles. Given that our model is based solely on the Kelvin equation and the geometric characteristics of the structure, our work not only shows a facile way to control capillary condensation for future applications, but also lends further support to the applicability of the Kelvin equation for systems containing sub-10-nm geometries.

By demonstrating a user-friendly way to control capillary condensation for a wide range of applications, our research provides new insights and possibilities in the field of porous materials. Furthermore, the successful application of the Kelvin equation to these advanced materials lends additional support to its relevance and adaptability in designing tailored porous structures. This pioneering work paves the way for the development of next-generation materials with enhanced properties, offering a solid foundation for future research and practical implementations in various industries.

4.0 A Synergistic Approach to Atmospheric Water Scavenging

This chapter is adapted from: Jiao, S. and McCarthy, J.J., 2023. A Synergistic Approach to Atmospheric Water Scavenging. *ACS Applied Materials & Interfaces*, *15*(5), pp.7353-7358.

An abundant supply of fresh water is one of the leading challenges of the 21st century[18]. Here we describe a new approach to scavenging atmospheric water that employs a hierarchically ordered porous material with embedded particles[126]. This composite uses structure to amplify native material performance to realize synergy between the capture and storage and ultimately qualitatively change the adsorption behavior of the hydrogel (from unfavorable to favorable). In this way we can capture moisture at significantly lower relative humidities than would otherwise be feasible with the native materials. Not only does this approach pose the potential for a cheap and low-energy source of clean water, but it could also be modified for application across a variety of condensible vapor reclamation.

4.1 Introduction

For decades researchers from across the globe have examined a variety of techniques for generating clean water[19] from desalination[20] to disinfection/decontamination[21,22]. More recently, a growing trend aims at harnessing the abundant supply of fresh water that is available within the atmosphere[1]. To date, such water scavenging approaches have largely leveraged daily heating/cooling cycles to overcome the energetic cost of condensation[3,4,127]. Some mimic the behavior of the desert beetle[5] to capture early-morning fog using, for example, synthetic netting[6]

or other biomimetic materials[128]. Another technique exploits solar energy more directly in order to enhance the release of water captured within a metal-organic framework (MOF) based sorbent material[8,9]. The approach espoused here, inspired by granular flows[14,129], employs a novel composite material capable of passive capture via a capillary condensation process with subsequent low-energy reclamation of the water through simple finger pressure. Despite the complex microstructure of the composite and nanometer-sized length-scales of the resultant contact spots[121], a continuum-based thermodynamic analysis accurately describes the observed results.

Even for particles that are hundreds of microns in diameter, surface asperities can cause aging of the material[14] that results in an increase in the static angle of repose of a granular bed (Figure 4.1a,b). This phenomena was quantitatively described by Bocquet et al. using the Kelvin equation[130] by attributing the angle increase to cohesion between the particles due to the capillary condensation of liquid bridges at the points of asperity contact. This tendency of particle imperfections to yield an order of magnitude decrease in the effective radius of curvature at contact spots is not only a boon to the longevity of sand castles[131], but it also forms the basis of the "capture" portion of our synergistic water scavenging approach.

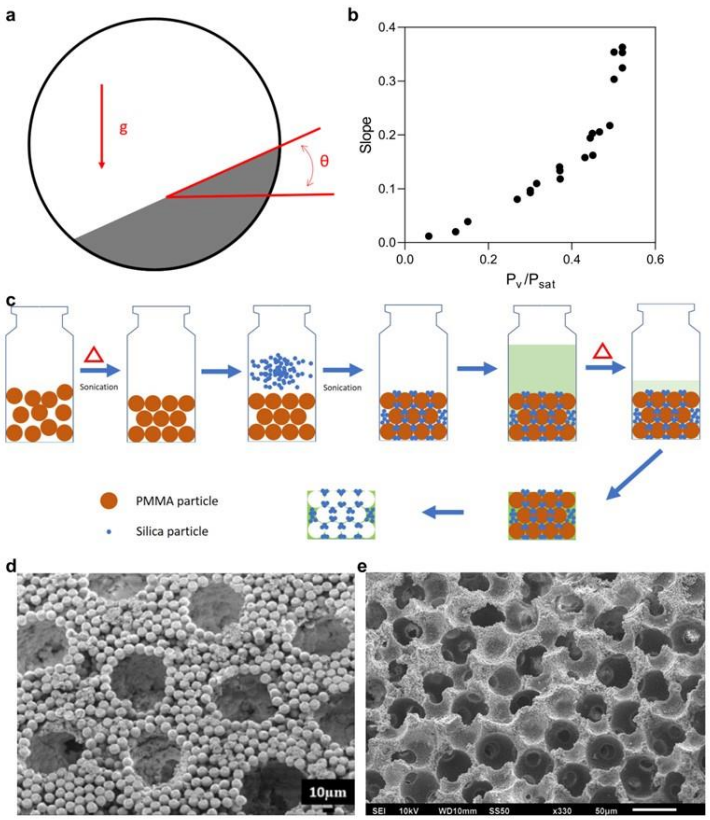

Figure 4.1 (a) Sketch of the rotating drum showing the avalanche angle θ. (b) As moisture condenses at the contact spots between particles, the avalanche angle increases. The bullets show the increase of the avalanche slope with increasing of RH (adapted from Ref. (Bocquet1998)). (c) Schematic of the synthesis of the composite. Sonication is used to form an ordered array of larger particles. Slight heating fuses the contact spots between large particles (ensuring future continuous void space). Small, hydrophilic particles then fill the interstices between the large particles. A hydrogel infuses the remaining voidage. When the large particles are selectively removed, a hierarchically-ordered porous composite remains. (d) SEM picture of the binary hierarchically-ordered particle matrix (when no hydrogel is used). (e) SEM picture of hierarchically-ordered particle matrix with hydrogel backbone (i.e. the composite).

It has long been recognized that nanometer-scale channels/curvature can nucleate capillary condensation[132,133] and it was recently shown that this phenomenon is quantitatively described by the Kelvin equation at scales even smaller than a nanometer[121]. Nevertheless, exploiting this relationship for water scavenging purposes is hampered by several factors, including the cost of nanoscale fabrication, the storage capacity of the nanostructured devices, and the ultimate recovery of liquid water that collects at the contact spots. In contrast, hydrogels have been recognized for decades as an outstanding storage medium for large quantities of (liquid) water[134], allow water recovery from simple compression/squeezing[135], and have even been shown to absorb a modest amount of moisture directly from vapor streams[136]. A thermodynamic view of the water uptake process is discussed in this chapter involving the water equilibrium between vapor phase and liquid phase of water in the system. Concurrently, similar efforts have been made by Liu et al.[137]where they discussed the equilibrium between a pure liquid solvent in a cavity and a gel, which is determined by the balance between capillarity and osmosis, known as the osmocapillary length. Their findings are in line with our analysis, and in this work, we further explore the equilibrium shift under the influence of external pressure.

4.2 Material and Methods

4.2.1 Preparation of the PHEMA Gel

We have evaluated several concentrations of the HEMA monomer from 20% to 60% in order to identify the optimum formula for the PHEMA hydrogel synthesis. For most of the

displayed results, a concentration of 25 wt% was used. The poly(hydroxyethyl methacrylate) gel monomer solution was prepared by homogenously mixing 75 wt% Deionized Water, 25 wt% 2-Hydroxyethyl methacrylate (99%; Sigma-Aldrich), 2.5 wt% ethylene glycol dimethacrylate (98%; Sigma-Aldrich) and 1 mg ammonium sulfate (99%; Sigma-Aldrich) and then the gel is prepared by heating the mixed monomer solution at 65 Celsius for 4 hours in a 2 ml glass vial.

4.2.2 Preparation of the Low-Porosity Pure Porous Gel

The 200 mg small PMMA particles (Cospheric; particles size ranges from 45-53 micron) and the 100 mg big PMMA particles (average particles size of 2 mm) were mixed in a 2 ml transparent glass vial, which was then heated at 210 Celsius for 30 minutes to fuse the mixed particle matrix. The 1 ml premixed monomer solution was injected into the matrix via syringe to decrease the infiltration time. The gelation was performed at 65 Celsius for 4 hours. Then the PMMA particles were dissolved in DCM (99.8%; Sigma-Aldrich) under stirring for 2 hours. Then the composite is freeze-dried under a high vacuum overnight.

4.2.3 Preparation of the High-Porosity Pure Porous Gel

The 200 mg small PMMA particles (Cospheric; particles size ranges from 45-53 micron) and the 100 mg big PMMA particles (average particles size of 2 mm) were mixed in a 2 ml transparent glass vial, which was then heated at 210 Celsius for 30 minutes to fuse the mixed particle matrix. The 200 mg silica particles (Sigma-Aldrich; average particle size of 3 micron) were then infiltrated into matrix via sonication. The 1 ml premixed monomer solution was injected

into the matrix via syringe to decrease the infiltration time. The gelation was performed at 65 Celsius for 4 hours. Then the PMMA particles were dissolved in DCM (99.8%; Sigma-Aldrich) under stirring for 2 hours. Then, the silica particles were removed via hydrofluoric acid etching. Finally the composite is freeze-dried under a high vacuum overnight.

4.2.4 Preparation of the Composite

The 200 mg small PMMA particles (Cospheric; particles size ranges from 45-53 micron) and the 100 mg big PMMA particles (average particles size of 2 mm) were mixed in a 2 ml transparent glass vial, which was then heated at 210 Celsius for 30 minutes to fuse the mixed particle matrix. The 200 mg silica particles (Sigma-Aldrich; average particle size of 3 micron) were then infiltrated into matrix via sonication. The 1 ml premixed monomer solution was injected into the matrix via syringe to decrease the infiltration time. The gelation was performed at 65 Celsius for 4 hours. Then the PMMA particles were dissolved in DCM (99.8%; Sigma-Aldrich) under stirring for 2 hours. Then the composite is freeze-dried under a high vacuum overnight.

4.2.5 Water-Uptake Isothermal Measurements

Relative humidity control was realized by putting dry air though a temperature-controlled water container. After bubbling through the water bath, the humidified air is fed directly to a glove box. For the water-uptake measurements, samples were dried under vacuum inside an opened airtight bag for 2 hours, while the humidity chamber reached desired relative humidity. Then the

airtight bags containing samples were transferred into the RH-controlled chamber. After desired time the bags were sealed, and the measurements were made using Mettler Toledo MS105DU.y

4.2.6 Absolute Dry Weight and Composite Composition Determination

The absolute dry weight of samples was determined by thermogravimetric analysis using TG/DTA200. The temperature was raised to 120 Celsius and held for an hour to allow fully water evaporation. And then the temperature was raised up to 600 Celsius and held for another hour to completely burn off any organic component (i.e., the hydrogel). The remaining mass was attributed to silica particles.

4.2.7 Characterization of Composite Structure

The quality of the hierarchical structure of the composites was observed using JEOL JSM6510 scanning electron microscope operating at 10 kV. All samples were coated with Pt using sputter coater before imaging.

4.3 Results and Discussion

The synergistic water-scavenging approach espoused here is comprised of materials that allow alternatively "capture" and "storage/release" of moisture. As such, the composite examined here uses a particle-based structure to create locations for capillary condensation, directly stores the water from the condensation spot in a continuous hydrogel, and allows water to be recovered

by simple methods such as hand squeezing. While the details are outlined in the Methods section included in the supplementary information (and illustrated in Figure 4.1c), based on the work of Lash et al[126]., we can create a hierarchically-ordered porous matrix that has a continuously-connected pore structure, a cross-linked poly hydroxyethyl methacrylate (pHEMA) hydrogel backbone, and an ordered array of densely-packed particles at the boundary of each pore wall (see Figure 4.1d and e). The idea behind our study is to examine the interplay between confinement-induced condensation and hydrogel swelling. As shown below, this cooperative behavior -- induced through structural design -- qualitatively changes the character and efficacy of water vapor absorption within the composite material, and can form the basis of a new class of condensible vapor scavengers.

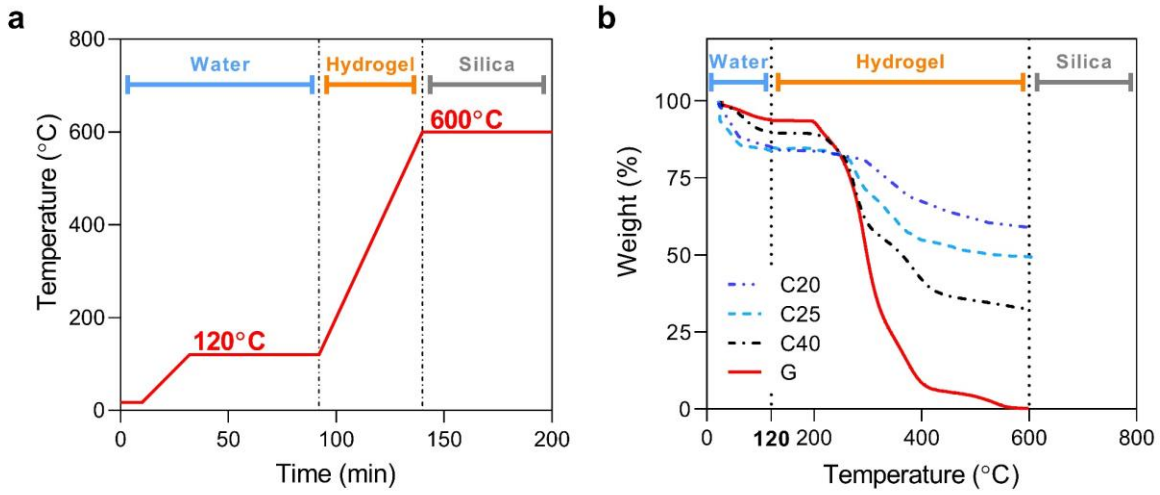

Figure 4.2 (a) The temperature ramping protocol used for Thermogravimetric Analysis (TGA) of the composite samples. (b) A series of TGA results for composites with different monomer concentrations and the pure hydrogel. The moisture content decreases and hydrogel content increases with increasing monomer concentration (ranging from 20% to 40%). The (red) solid line represents the thermal degradation curve of the pure hydrogel. The (blue) dash-dotted line, (blue) dashed line, and dash-dotted line represent the thermal degradation curves of the composites containing 20%, 25% and 40% monomer concentration hydrogel, respectively. Based on these results, the composite containing a 25% monomer concentration hydrogel is used in the remainder of the study as a compromise between water absorption and structural integrity.

In order to test the water-adsorptive capacity of our composite, we use a humidity-controlled glove box. The material to be tested is placed in the box under different relative humidity environments, ranging from 15% to 90%. For each measurement, the sample was allowed to approach equilibrium over the course of a 2 day exposure. Figure 4.3a shows that, for a relative humidity of 35%, a 48 hour exposure is sufficient to realize the asymptotic adsorption within the material. In addition to testing a variety of realizations of our composite material, as a control, we also tested several samples of porous PHEMA gel (see Methods section for the fabrication technique of both a high and low surface area porous gel; note that in each of these samples we have omitted the small silica particles). The mass of all tested samples are measured both pre- and post-exposure (with samples sealed in an airtight bag for transport between the humidity chamber and scale). The samples were further evaluated using a Thermogravimetric Analysis method (TGA) in order to ascertain the absolute dry weight and composition of gel and silica particles within each sample (see Figure 4.2 and the Methods section for the TGA protocol). The absorptive performance is quantified based on the mass of water absorbed relative to both the mass of the total amount of hydrogel in that composite (in order to highlight the impact of structure on absorption) as well as the mass of the full composite (in order to point toward future device efficiency).

In Figure 4.3b, it can be seen that, under typical atmospheric conditions, the composite can recover from an ambient gas source nearly 80% of the water that would have been available from a liquid source (143% of the hydrogel weight, obtained by fully swollen the hydrogel in water). In contrast, the porous PHEMA hydrogel (as the control) can only achieve less than half of the maximum absorption under the same humidity conditions. More significantly, for the composite, there is a sharp increase of water uptake observed near a relative humidity of between 25-30%,

while the absorption of the control is far more gradual, thus the control achieves an extremely low uptake at relative humidities below 50%.

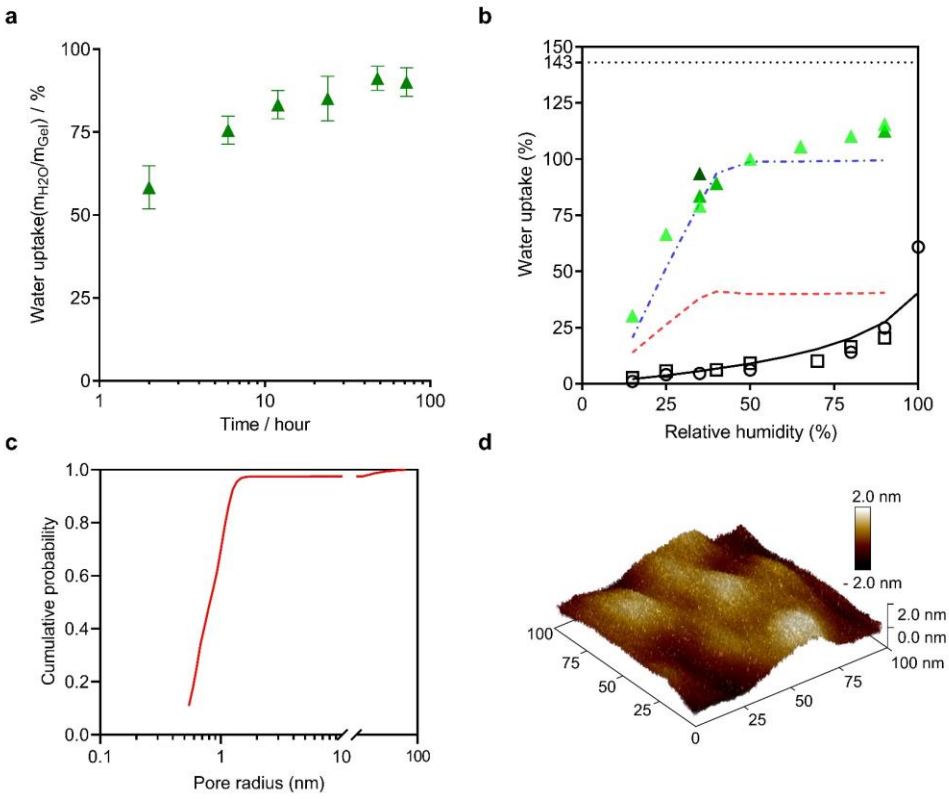

Figure 4.3 (a) Water uptake of the composite when exposed to a 35% relative humidity (RH) environment over a period of many hours. We define water uptake as the ratio of absorbed water mass to hydrogel mass, expressed as a percentage. (b) Water retention isotherms for the composite (multiple results are presented) and pure porous PHEMA hydrogel and their corresponding theoretical curves when samples are exposed to vapors of varying RH for 48 hours. Note that an immersed sample of pure hydrogel absorbs 143% of its own mass (shown as a dotted line). Open circles and squares represent a low and high porosity hydrogel sample, while (green) triangles represent composite results (with two darker shades corresponding to additional composite trials). The solid line represents the thermodynamic predictions of hydrogel-based vapor absorption, while the (red) dashed and (blue) dash-dotted line show the results from the composite theory and composite theory with pore filling, respectively. (c) Brunauer-Emmett-Teller (BET) surface area analysis for a composite sample, showing the cumulative distribution function (CDF) of pore sizes. (d) An atomic force microscope (AFM) image of a 100 nm^2 surface of a representative silica particle. Note that surface asperities include imperfections in the range of 1 nm in size.

According to Flory – Huggins theory[138,139], the equilibrium swelling of a crosslinked polymer network can be represented by:

$$\frac{\partial \Delta G}{\partial n_l} = RT\{\ln(1-\phi_g) + \phi_g + \mathcal{X}\cdot\phi_g^2\} + v_e v_l RT\phi_g^{\frac{1}{3}} \qquad \textbf{Eq(4.1)}$$

Where delta G is the Gibbs free energy change, R is the gas constant, T is the temperature, ϕ_g is the volume fraction of the gel in the mixture, $\mathcal{X}$ is the Flory-Huggins parameter, n_l are the moles of the solvent, v_l is the molar volume of the solvent and v_e is the moles of chains per volume.

In the case when water vapor is the source of the swelling solvent, and is therefore in equilibrium with the swollen hydrogel, an additional term is required leading to a complete thermodynamic relationship for water absorption as shown below:

$$\frac{\partial \Delta G}{\partial n_l} = RT\{\ln(1-\phi_g) + \phi_g + \mathcal{X}\cdot\phi_g^2\} + v_e v_l RT\phi_g^{\frac{1}{3}} - RTln\left(\frac{P}{P_{Sat}}\right) \qquad \textbf{Eq(4.2)}$$

For our control samples, we can estimate the water volume fraction (hence the water uptake) at equilibrium by setting the free energy change to zero. Using a nonlinear curve fit for both the Flory-Huggins parameter, $\mathcal{X}$, as well as the chain density, v_e, using the experimental data for the porous pure PHEMA hydrogel experiment data (See Figure 4.3b, black line) we obtain the parameters of $\mathcal{X}$ as 1.05 and v_e as 1.25e-4 mols/ml. In order to use this model for our composite material, we must recognize that the nucleation sites for capillary condensation that are inherent in the structure of our material will alter the vapor-equilibrium term of this equation. That is, we must use the Kelvin equation near nucleation sites so that we modify the effective location saturation pressure from that of the "flat" value (P_{Sat}) to that of the curved value (P_{Sat}^{c})

$$\frac{\gamma_{lv}}{r} = \rho_1 k_B T \ln\left(\frac{P_{Sat}}{P^c_{Sat}}\right) \qquad \textbf{Eq(4.3)}$$

Here, r represents the radius of the curvature near the contact spots. Using this equation, we note the critical curvature values, r_c, that would result in an effective local relative humidity of 100% (i.e., for non-confined relative humidities below 50%, we require condensation spots in our composite that have a radius of curvature less than 1.5nm). Using a Brunauer–Emmett–Teller (BET) measurement of our composite, we find the pore size distribution of the composite. Figure 4.3c confirms that most of the pores in the composite have a diameter less than 1.5nm. Moreover, an Atomic Force Microscope (AFM) image (Figure 4.3d) of the surface of our silica particle inclusions, confirms the asperity scale to coincide with this size. By assuming that these pores are uniformly distributed throughout the composite, we can apply our simple thermodynamic approach using a non-confined relative humidity for the fractions of the composite whose pore curvatures, r, are larger than the critical value, r_c but instead assume saturated conditions for the fractions where $r < r_c$. The (red) dashed curve in Figure 4.4a,b show the qualitative change in absorption behavior under these conditions. Despite this modification to our theoretical approach, there remains a quantitative difference between the experimental measurements (triangles) and this modified theory (Figure 4.4a,b). This discrepancy stems from the lack of consideration of free moisture filling the pore spaces near the condensation spots. That is, the modified theory allows for hydrogel equilibration with free moisture, but the model does not account for the remaining free moisture. In order to estimate the amount of water trapped by filling the (correctly-sized) pore spaces with free moisture we again turn to the measurement of the cumulative pore size distribution (Figure 4.3c). By using the fraction of the total open pore volume that has curvature sufficient to induce free moisture condensation, along with the experimental measurement of the swelling ratio

(i.e., the product of the gel density and the maximum water uptake, which yields 1.65 grams of water per milliliter of gel) we are able to calculate the free moisture trapped within the pore spaces at each relative humidity (shown as the (blue) dash-dotted line in Figure 4.3b). Note that, by accounting for both effects of the local confinement we obtain a modified model that matches experimental measurements quite closely.

To confirm that the increased water uptake is not simply attributable to the excess pore-filling outlined in Figure 4.3b, we conducted a sequence of ‘‘component" tests, as follows. We first tested the bare pHEMA hydrogel under 93%RH. Under these conditions, the hydrogel absorbed 101.9 mg of water, representing 13.21% of its dry mass (which was 771.4 mg). Similarly, when we deposited a layer of bare silica particles onto a silicon wafer, the system absorbed 3.5 mg of water, representing 219% of the particles' (dry) mass (which was 1.6 mg). We then combine these two components by forming a pHEMA hydrogel film on top of particles that were deposited on the silicon wafer and peel off the film to expose a composite surface to the moist air. A naive superposition of the component absorptions would suggest that this composite would yield 41.4 mg of water (based on the absorption expected from the 1.6 mg of particles embedded in 286.8 mg of pHEMA). Interesting, we instead observe that this composite film absorbs 68.2 mg, so that the synergistic effect of combining the moisture capture and storage yields a 65% increase in absorption efficacy.

As the final factor in understanding the behavior of our composite, we must investigate the response of the system to externally-applied stress/pressure. Here, we introduce a stress term to our modified theoretical treatment Π.[138,139] The inclusion of an external stress changes the chemical potential of the solvent so that the relationship between the applied stress and the volume fraction of the gel at equilibrium is now expressed as

$$\Pi v_l = RT\left\{\ln\left[(1-\phi_g)(\frac{p_v}{P})\right] + \phi_g + \chi\cdot\phi_g^2\right\} + v_e RT v_l \phi_g^{\frac{1}{3}} \qquad \textbf{Eq(4.4)}$$

Figure 4.4a shows the relationship between the applied stress and the hydrogel volume fraction for a series of relative humidity values. By comparing the change in the volume fraction of the hydrogel between no externally-applied stress (0 pa) and an estimate of hand grip pressure (10^7 Pa)[140] suggest the amount of water that can be recovered by squeezing the sample. As can be seen from this analysis, with an increase of RH, the amount of water that can be recovered (i.e., the shaded area) increases. Comparing the experimental values to those predicted from this analysis shows substantial agreement from the samples of pure, porous hydrogel (open circles and the solid line, respectively). In order to analyze the composite, we apply the modified theory with both unstressed and hand-grip pressure to obtain the (blue) dash-dotted line. Note that, due to the very high Laplace pressures within most of the highly-confined pore spaces, we assume that water is expelled almost exclusively from the hydrogel itself rather than from the pores (with the exception of the pores above 5nm where the hand-grip pressure exceeds the Laplace pressure).

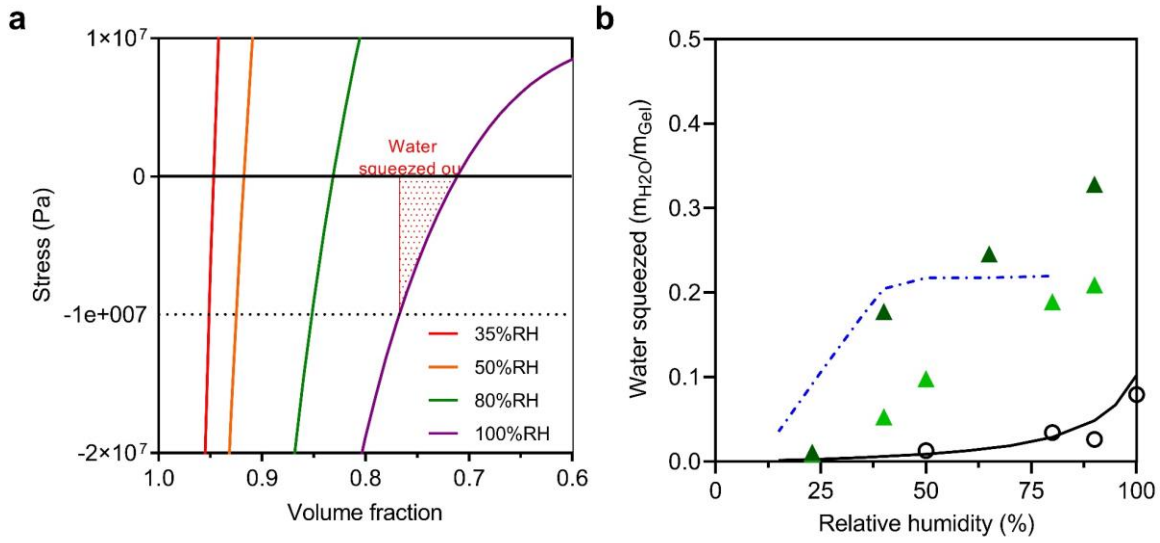

Figure 4.4 (a) Theoretical relationship between applied pressure and hydrogel volume fraction for a series of relative humidities (humidity increases for curves from left to right) based on the thermodynamic analysis included in the text. Note that water uptake (in volume fraction units) may be obtained from the 0 Pa stress crossing, while water expulsion upon squeezing is obtained from negative stress values (here taken to be approximately -7x10^7 Pa). (b) Mass fraction of water squeezed out of both composite and hydrogel samples, under different relative humidity (RH) environments. Here we express results as a ratio of the mass of water expulsion to the hydrogel mass. Open circles represent a pure porous hydrogel sample, while (green) triangles represent two realizations of composite material. As in Figure 4.3, the solid line corresponds to the thermodynamic analysis, while the (blue) dash-dotted line represents the modified version applicable to the composite.

4.4 Conclusion

Our composite shows great potential for scavenging of ambient water vapor and other condensable vapors in an economical, environmentally friendly, and remarkably simple way. The absorption process is completely passive in that it doesn’t require external energy, special equipment or any particular environmental conditions in order to function. Compared to most existing approaches using current absorbents, it is the structure of our composite that leads to a qualitative change in the absorption behavior of the ultimate material. This new structure greatly increases the efficiency of absorption when compared to the native material. Thus, the same central idea, that structure can be used to amplify native material performance, may be applicable to a variety of adsorbent materials. Even without optimization of the composite or fabrication, we note that up to 5% of the composite's mass is easily recoverable at humidities below 50% from materials that are extremely abundant and inexpensive.

5.0 Modeling of Particle-Particle and Particle-Fluid Interactions in a Fluidic Environment

This Chapter expands upon the application-driven research in Chapter 3.0 to computationally explore a potential fabrication method for the creation of particle-based crystalline materials by exploiting viscosity-base hydrodynamic interactions. All our composites and samples are based on particle-based or inverted particle-based crystals. This type of material has garnered substantial recent attention within the literature both with respect to fabrication techniques as well as in exploration of their suitability in a variety of applications. In this chapter, with the help of an advanced LBM-DEM simulation method, we explore the particle-particle, and particle-fluid interactions exhibited in a density-matched fluid-particle environment. We hope to exploit these interactions as a means of paving the way for scale-up composite fabrication or for creation of a more advanced *in situ* particle-based crystal fabrication technique.

5.1 Introduction

Among all the techniques of forming ordered porous materials, colloidal crystal templating is one of the most promising techniques that are still under development[94,95]. Colloidal particles, typically monodispersed and spherical, are considered as building blocks to form, via self-assembly, particle-based crystalline materials[96]. These crystals are either directly used as porous materials by themselves, with additional treatment to overcome the brittleness of the close-packed lattice, or can be used as templates to form porous materials via their interstices[97–99]. With the

enhancement of our understanding of colloidal self-assembly, we are able to form complex structures with hierarchically ordered colloidal crystals using multi-size particles. The recent work in our lab[141], as well as elsewhere[142–148], has shown the ability to create binary colloidal templates using different techniques and forming inverse structures with multi-scale pores.

During the creation of our composite in previous work[149], we noticed that certain experimental conditions would result in external agitation causing the formation of a closely-packed structure via a self-assembly process; however, due to limitations of the available experimental equipment, we could not realize diligent/precise control of the external agitation in order to elucidate the precise conditions that would lead to these results. Here, we utilize a well-developed mathematical simulation model to explore the particle interactions under different external agitations, as well as the possibility of scaling up the suspension self-assembly technique.

Computational fluid dynamics (CFD) is a set of well-studied numerical methods for the simulation of fluid, and fluid-particle, motion. With the increase in computing power and the growth of research in the simulation field, CFD has been getting increased attention due to its accurate and effective prediction of the behavior of complex fluid dynamics[110]. The Lattice Boltzmann method (LBM) is a growing approach espoused with the overall class of CFD methods. It allows extreme flexibility in the treatment of complex boundary geometries and fluid-boundary flow conditions. LBM recovers the Navier-Stokes equations by using the Chapman-Enskog expansion[150], making it easy to discretize in a rectangular grid. LBM consists of two computational steps: streaming and collision, that basically simulate the advective transport of momentum as well as the interactions with neighboring fluid elements, respectively.

The Discrete Element Method (DEM) is the most widely used simulation method for capturing the Lagrangian motion of particle entities. It captures the motion of every particle in an

extensive system by direct calculation and integration of Newton's law of motion. Particle properties such as size, density, and shape can be easily specified. For each time step, the velocity and position of each particle in the system are simulated and recorded. The simulation also captures the values and time-series of forces applied to the particles, including such forces as gravitational, frictional, and adhesive forces.

Here, we used LBM coupled with DEM to simulate particle interactions under external agitations in a liquid environment.

5.2 Code Validation

In this work, the LBM method is used to capture the fluid behavior; the DEM method is used to capture the particle motion and is coupled to the LBM method in order to consider the momentum transportation between the fluid and particle phases. In this section, a few validation studies are performed to demonstrate the capability of our LBM-DEM numerical approach to simulate particle and fluid behavior in a particle suspension environment, including two-particle collisions and particle collisions under external energy agitation.

5.2.1 Two Particle Collision

The collision of particles has been a subject of ongoing interest for years. While many of the studies focus on the dry collision process[151], a few studies have included how an interstitial fluid influences the collision process[152]. It is our interest to study particle-particle interactions in

the presence of an interstitial liquid. Thus, validating our model for two-particle collisions submersed in fluid media is a great start.

We set up a series of simulations to verify that our LBM-DEM model can realistically reflect the observed experimental behavior when two particles collide in a liquid suspension. Our simulation is carried out in a cubic tank filled with liquid. The size of the tank is set as 100x100x100 mm. Two identical spherical particles with densities that match that of the liquid and have a diameter of 5 mm are put near the centerline of the tank at a separation distance of 5 mm (i.e., one particle diameter apart), as shown in Figure 5.1 Different initial speeds were given to both particles in the opposite direction so they would move directly toward each other. During the simulation, since we only provided initial speeds to the particles, the total energy of the two-particle system was constantly dissipating into the fluid. Thus, we set the initial velocity in a way that the minimum speed would at least induce a collision, and the maximum speed would be sufficient that the two particles bounce away from each other after their interaction.

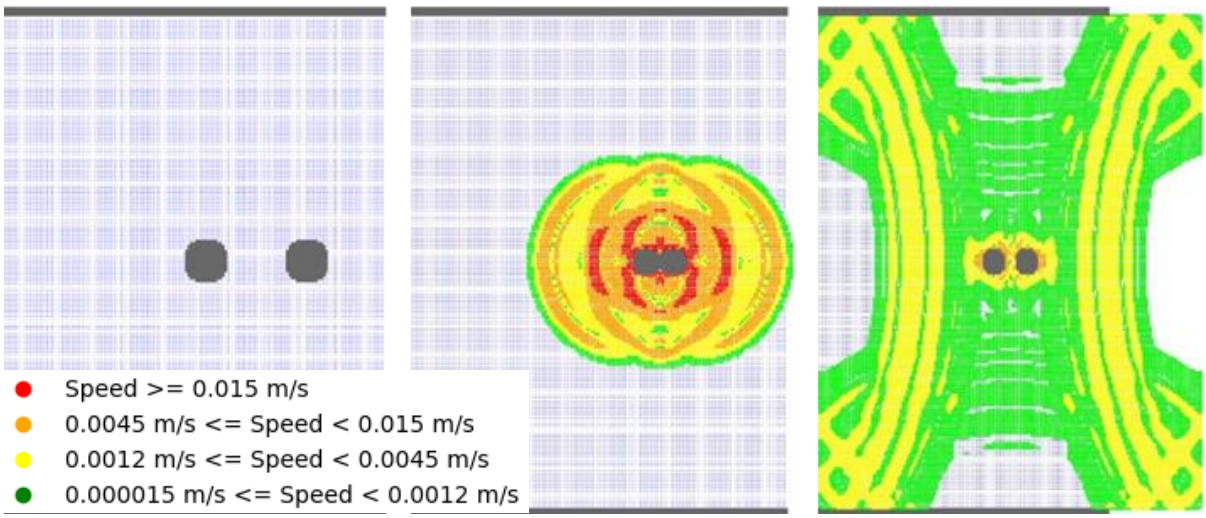

Figure 5.1 A series of snapshots showing a two-particle collision process simulated using our LBM-DEM method. The simulation is carried out in a cubic tank filled with liquid. The size of the tank is set as 100x100x100 mm. Two identical spherical particles with densities that match that of the liquid and a diameter of 5 mm are put inside the tank at a distance of 5 mm (i.e., one particle diameter apart) on the same level. A velocity heatmap is used to visualize the momentum of each node in the simulation.

To assess the simulation quality, we introduce a critical parameter: The Stokes number, St, is the dimensionless number that compares the inertial force of the particle with the viscous force of the fluid, and is written as

$$St = \frac{\rho_p w_p d}{9\rho\nu} \qquad \textbf{Eq(5.1)}$$

where ρ_p is the particle density, ρ is the fluid density, w_p is the particle velocity, d is the particle diameter, and ν is the kinematic viscosity. The Stokes number is often used as the pertinent number to characterize a particle collision with a surface such as a wall[152–154]. In general, for low St numbers, the particle does not rebound from surfaces, as the initial inertial energy of the particle is entirely dissipated into the fluid via viscous interactions (and the pre-collisional inertial energy that is stored as elastic energy during the solid (collisional) deformation is insufficient to allow rebound). Thus, a critical St number (St_c) exists that, for $St > St_c$, the particle shows a bouncing/rebound motion. Note that the value of St_c depends on the properties of the solid matter and the simulation setup[155–158].

In the case of a two-body system (i.e., two particles are involved in the collision), the St number represents a measure of the inertia of the colliding particles relative to the viscous force of the surrounding fluid and can be rewritten[159] as

$$St = \frac{\tilde{m} v_0}{6\pi\mu\tilde{a}^2} \qquad \textbf{Eq(5.2)}$$

Here, $\tilde{m}$ is the reduced mass of the particles ($\tilde{m} = \frac{m_1 m_2}{m_1 + m_2}$), where subscripts indicate different particles), v_0 is the initial relative velocity between the two particles, μ is the viscosity of the liquid, and $\tilde{a}$ is the reduced radius of the particles ($\tilde{a} = \frac{a_1 a_2}{a_1 + a_2}$).

Furthermore, to validate the consistency of our LBM-DEM model, we tested our model for two-particle collision under three different fluid viscosities. For each viscosity, both particles were given a series of initial velocities. And the initial St number was calculated for each case. Table 1 shows the critical Stokes number, St_c, for each viscosity.

Table 1 Kinematic viscosity settings for two-particle collision simulation

Kinematic viscosity m^2/s	1.0533E-07	2.00E-07	5.00E-08
St_c	15.82329	13.888889	13.888889

As one can see, the critical Stokes numbers are consistent across different viscosities, proving our model's reliability. The critical St value also aligns with findings from other research. For instance, Gondret et al.[152] conducted an experimental study on the bouncing motion of solid spheres colliding with a solid plate, which yielded a critical St value of approximately 10..

5.2.2 Particles in a Fixed Initial Position

To further test our model under more complex situations, we create a particle suspension system with 100 particles in a density-matched solution. To simplify the simulation and for easy observation, we create an initial arrangement of particles such that the position of each particle is such that every particle is one diameter apart from others (i.e., the center-to-center distance of two particles is two diameters). The external energy to agitate the system is introduced by moving the top plate of the system by employing an oscillatory motion. In this way, we can examine a finite-

sized system whereby the (simple) fluid streamlines vary in a periodic way that ensures that streamlines cross at differing times of the flow (a condition of good mixing in a low-Reynolds number, 2D flow)[160]. By varying the amplitude and frequency of the top plate's oscillatory motion, we are able to find a suitable protocol to drive desired flow and mixing patterns that lead to interparticle collisions.

Figure 5.2 shows a series of both 2D and 3D visualizations from a simulation with the top plate moving with an oscillatory motion where the maximum speed of the wall is 2 mm/s and the frequency of direction-switching is 0.02π. One can notice particle collisions are induced under this protocol and local particle density can be induced to increase with time under proper flow conditions.

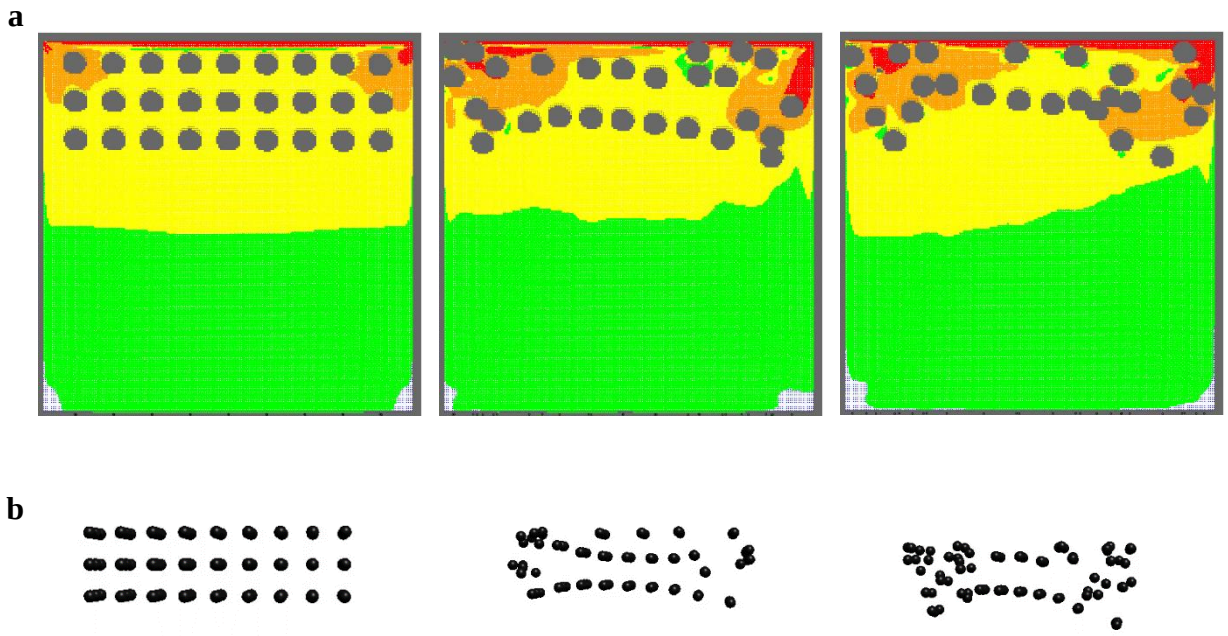

Figure 5.2 A series of 2D(a) and 3D(b) simulation snapshots with the top plate moving with an oscillatory motion at a top speed of 2mm/s and a frequency of 0.02 π . The external energy to agitate the fluidic motion and particle collisions is introduced by moving the top plate of the system at an oscillatory motion.

5.3 Simulation Set Up

Finally, to examine the impact of varying flow conditions on the local variations of particle density, we set up a system where the particles are randomly placed within the simulation area. In order to keep the computation achievable, the simulation area is restricted to a cuboid system. One hundred monodisperse particles are randomly placed in the domain at the beginning of the simulation, as shown in Figure 5.3. And the domain is filled with density-matched fluid to counter the gravity effect on the particles. The background flow information and the top plate motion are given in Table 2. Please note that even though all the particles are randomly placed, we have to set a minimum distance of two particles to be at least one diameter for our simulation to run smoothly and to ensure that no anomalous collision behavior is observed.

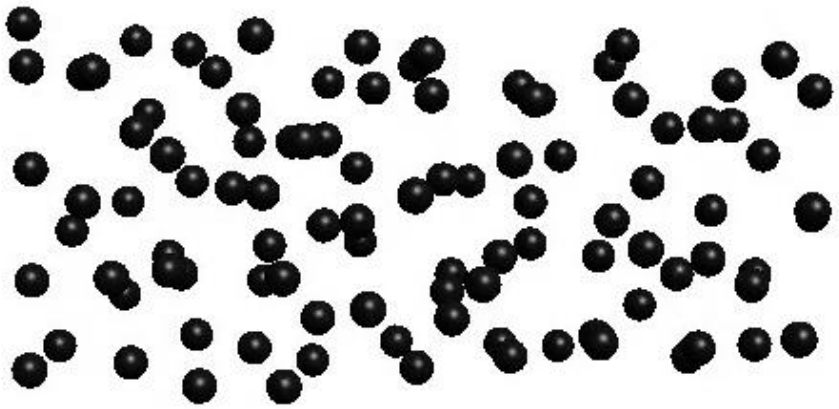

Figure 5.3 An illustration of the system setup. One hundred monodisperse particles are randomly placed in the domain at the beginning of the simulation. And the domain is filled with density-matched fluid to counter the gravity effect on the particles.

Table 2 Parameters of the simulation setup

Grid Resolution N^3	200x100x100
Nodes Per Particle	10
Kinematic Viscosity of Fluid (m^2/s)	0.0000005
Velocity Of the Wall (m/s)	Vmax*sin (0.02*pi*t)
Vmax	0.01, 0.02, 0.03, 0.04

5.4 Characterization of the Simulation Results

The radial distribution function is one of the most used methods for characterizing particle dynamics and particle clusters in flow[161]. Since the rise of the century-old idea, it has been widely used in various fields such as geometry[162], astrophysics[163], granular materials[164], crystallography[165], and plasma physics[166]. The RDF introduces a pair correlation function that quantifies the spatial correlation of density fluctuations. In the context of characterizing particle clusters, the spatial coordinates of each member within a group of particles are determined. Subsequently, the RDF measures the probability of locating a particle at a specific distance from a reference particle. Consequently, by utilizing the RDF, we can analyze complex 3D particle systems, gain insights into cluster structures, and determine the number of particles within a particular region.

In this specific situation, we first create a conceptional concentric spherical shell with a thickness of 2Δr around a central particle. The volume of such a shell, V_{Shell}, is given by.

$$V_{\text{Shell}}(r,\ \Delta r) = \frac{4}{3}\cdot\pi\cdot\left[\left(r + \frac{\Delta r}{2}\right)^3 - \left(r - \frac{\Delta r}{2}\right)^3\right] \qquad \textbf{Eq(5.3)}$$

In making this volume calculation, it is important to note that, when the spherical shell intersects the cuboid boundaries, the volume of the shell needs to be adjusted to account for the volume that remains inside the cuboid to give the correct RDF calculation, as shown in a 2D illustration in Figure 5.4. Here, we adapted an analytic approach from Kopera[167], who provided the quantitative analysis of the remaining volume of a shell intersecting the cuboid boundaries.

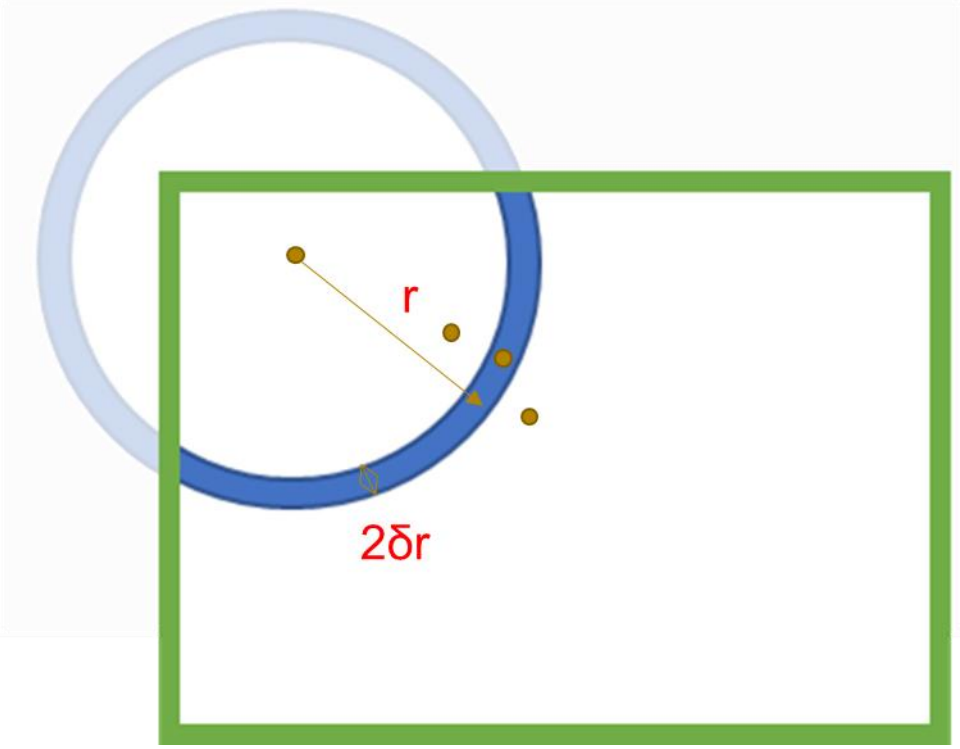

Figure 5.4 2D illustration of the conceptional concentric spherical shell with a thickness of 2Δr and a radius of r to the central particle. When the spherical shell intersects the cuboid boundaries, the volume of the shell needs to be adjusted to the volume that remains inside the cuboid to give the correct RDF calculation.

Using the properly calculated shell volumes, the radial distribution function, g(r), can be algorithmically written[168] as,

$$g(r) = \sum_{i=1}^{N} \frac{\psi_i(r)/N}{(N-1)\left(\frac{dV_r}{V}\right)}, \qquad \textbf{Eq(5.4)}$$

Where $\psi_i(r)$ is a count of the number of particles having their centers a distance $r \pm \Delta r$ from the center of the ith particle in the system (i.e., in the ith spherical shell), N is the total number of particles in the system, and V is the total volume of the system. As one can see in the equation, the radial distribution is normalized by the average particle density in the system, which means g(r) should approach a value of 1 as r approaches infinity.

5.5 Results and Discussion

The energy driving the motion of both fluid and particles originates from the oscillation of the top plate. To investigate the effects of external agitation on fluid movement and particle motion and collisions, we examine different movement patterns of the top plate. Specifically, we modify the amplitude and frequency of the sine function employed to dictate the top plate movement in order to achieve the most effective agglomeration.

First, we test various frequencies to optimize the output. If the frequency is too low, the flow approximates a simple cavity flow and the particles are simply carried with the fluid in its concentric streamlines. Given that the particles are initially placed relatively close to the top plate (where many of the concentric streamlines are in close proximity), the flow carries the particles to move along the edges of the domain, as shown in Figure 5.5b. As such, the particles largely trace

the fluid motion and there is little opportunity for the close particle approach necessary for particle agglomeration. Conversely, with a high frequency, insufficient momentum penetrates deep into the system, leading to minimal particle motion, collisions, and agglomeration, as demonstrated in Figure 5.5a. Similar outcomes are observed with regard to the maximum wall velocity. If the wall velocity is too high, particles are swept away by the powerful flow induced by wall movements. If the wall velocity is too low, there is inadequate momentum introduced to stimulate particle collisions.

After experimenting with different flow protocols, we opt for a frequency of 0.02 Hz, as it yields optimal results and functions effectively with a wide range of amplitudes, promoting particle agglomerations for further model testing.

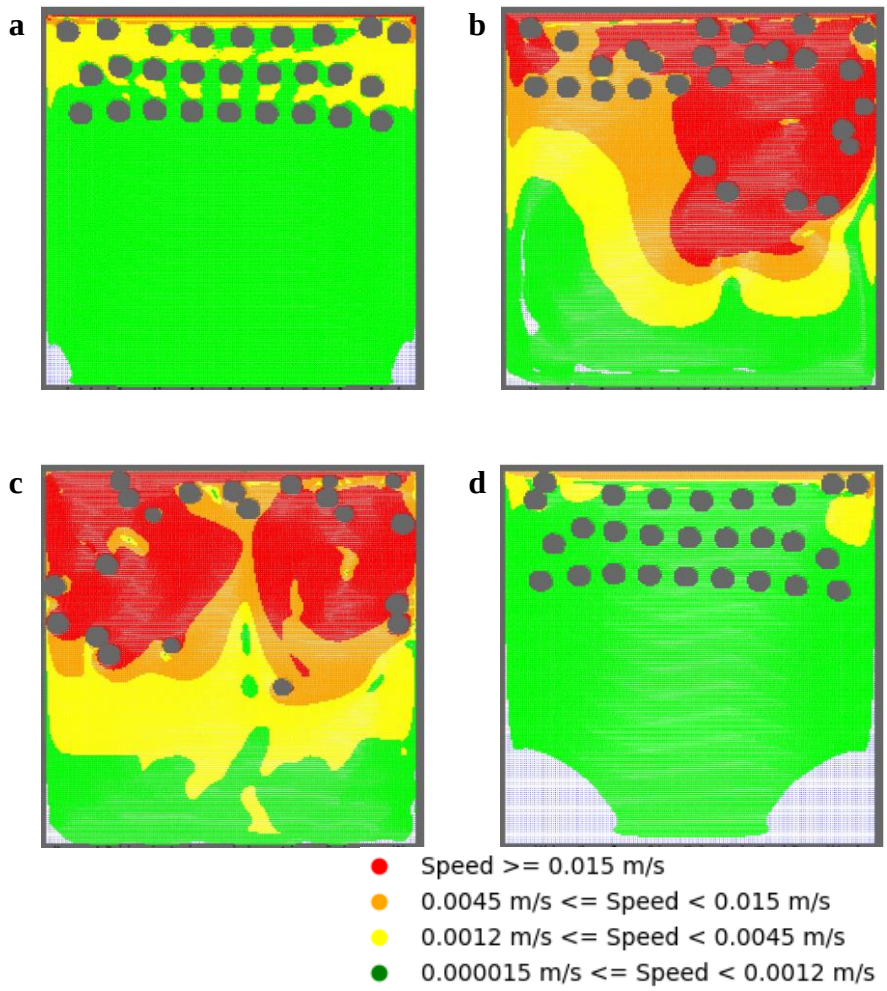

Figure 5.5 Simulation snapshots with four extreme situations: the frequency of the wall movement is too high (a) or too low (b); the wall velocity of the wall is too high (c) or too low (d). If the frequency is too low, considerable momentum is built up in a single direction, and the strong flow carries all the particles to move along the edges of the domain. This intense fluidic motion heavily influences particle movement and is not conducive to ideal particle agglomeration. Conversely, with a high frequency, insufficient momentum is introduced to the system, leading to minimal particle motion, collisions, and agglomeration. Similar outcomes are observed with regard to the maximum wall velocity. If the wall velocity is too high, particles are swept away by the powerful flow induced by wall movements. If the wall velocity is too low, there is inadequate momentum introduced to stimulate particle collisions.

The sine function's amplitude, which determines the top wall's maximum velocity, governs the total energy input as agitation within the system. The different amplitude changes the system's kinetic energy, influences the fluid's momentum build-up, and ultimately impacts the collision frequency and velocity of the particles in the system.

5.5.1 Collision Duration Analysis

In order to explore the impact of the external agitation protocol on particle agglomeration, four different maximum top wall velocities are tested in our model: 0.5 mm/s, 2 mm/s, 3 mm/s, 4 mm/s. To better understand the collision process in each case, we record every event (i.e., a "collision") in which particles achieve close proximity (within a half-diameter) as a function of time and, further, we note the duration of time in which the particles remain in proximity. When this information is gathered on a plot, we call it a "collision map". Figure 5.6 presents the collision map for all four settings. Each point on the figure represents a single collision event, signifying that a specific pair of particles have approached each other to within a half-diameter. The x-axis represents the dimensionless simulation time in which this collision concludes (i.e., when the particles have separated by more than the critical amount), while the y-axis value indicates the duration of each collision event. For example, a point at (800, 200) represents a single collision event occurring from the 600th to the 800th simulation time step.

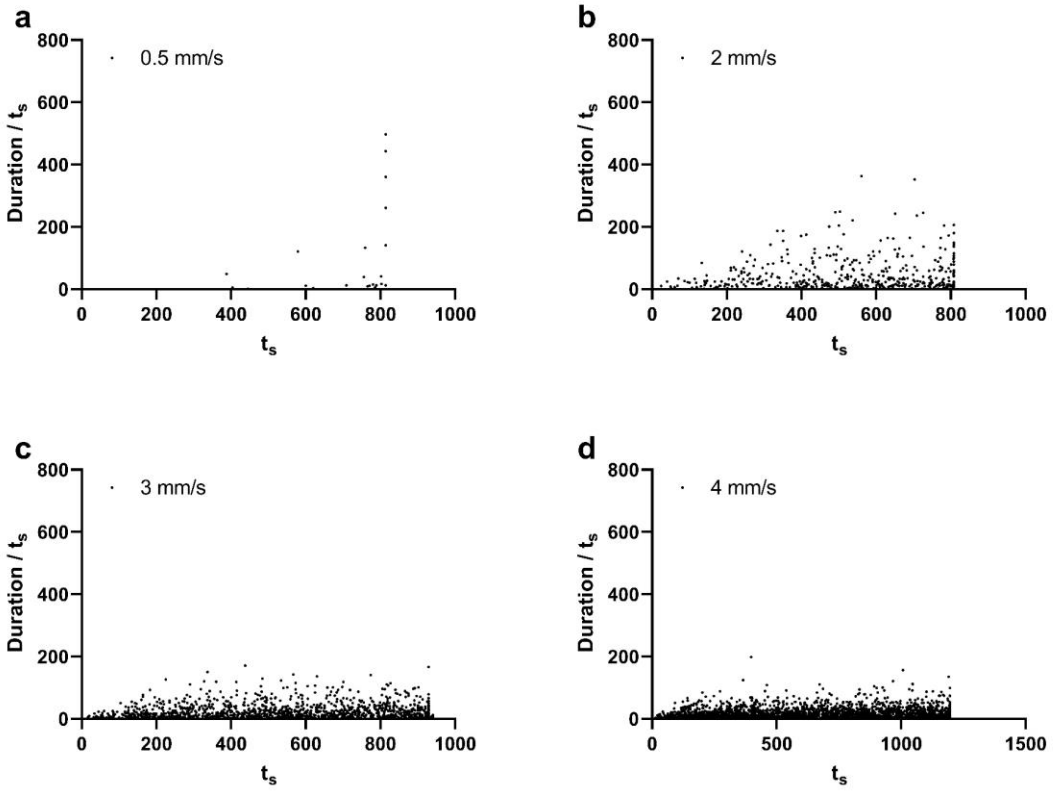

Figure 5.6 The collision map of different simulation settings. Four different maximum top wall velocities are tested in our model: 0.5 mm/s, 2 mm/s, 3 mm/s, 4 mm/s. The x-axis represents the simulation time step, indicating the end simulation time step of each collision event, while the y-axis displays the duration of each collision event.

As one can see, as the maximum velocity of the top wall (i.e., the amplitude) increases, there is an increase in the density of the points in the collision map. This suggests that the number of collisions happening over the same period of time increases. This suggests that the protocol chosen effectively induces mixing so that particles have the opportunity to explore different portions of the flow. Moreover, with an increase of the maximum wall velocity, the rapidity with which this mixing occurs creates more opportunities for particle collisions to occur.

On the other hand, among all the collisions happening in the different experiments, the average length of the collision duration decreases as the maximum wall speed increases. For example, as seen in Figure 5.6, while the 0.5 mm/s driving velocity causes very few collisions some of them last for nearly the entirety of the simulation. Similarly, the 2mm/s driving velocity clearly induces some collisions that endure for nearly 400 simulation units, but the more rapid driving velocity does not exhibit similarly long collision durations. As another way of examining this phenomenon, Figure 5.7 shows the duration distribution of 2mm/s, 3 mm/s, and 4mm/s simulations. Note that 0.5 mm/s is not included in the analysis due to the ultra-low total collision counts. It can be seen that as the maximum wall velocity increases, the duration of the particle collisions is highly concentrated below 50 time units, while slower maximum wall velocity yields wider distribution with longer durations.

It is also interesting to note that for the simulations of 3 mm/s and 4 mm/s, the simulation seems to enter a steady state, as suggested by the recurring pattern of the collision counts and duration; however, for the simulation of 2 mm/s, it seems that the duration of collisions and frequency are both increasing with the simulation length.

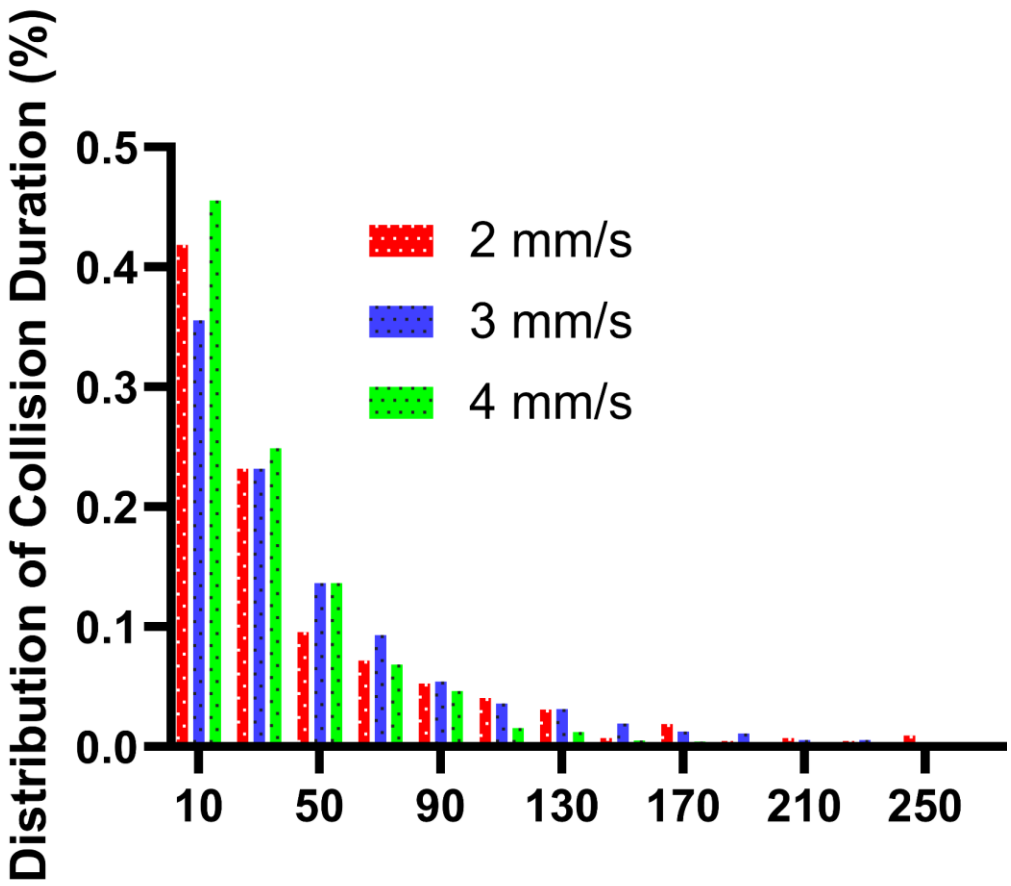

Figure 5.7 Collision duration distribution of 2mm/s, 3 mm/s, and 4mm/s simulaitions. The Y-axis shows the relative percentages of certain collision durations compared to the entire range of duration variations.

5.5.2 Radial Distribution Function Analysis

Revisiting the radial distribution functions (RDFs) as an alternative means of understanding particle clustering, we performed these analyses across all simulation cases. In the study of radial distribution functions (RDFs), Ri and Rp designate the radii of two distinct entities involved in the analysis. Ri refers to the radius of a spherical shell centered around a reference particle, while Rp represents the radius of the reference particle itself. During the investigation of RDFs, the Ri/Rp ratio is frequently examined to offer insights into the system's relative spatial distribution of particles. A peak in the RDF plot at a particular Ri/Rp value signifies an increased probability of encountering particles within the spherical shell of radius Ri, centered around the reference particle with radius Rp. Figure 5.8 illustrates the RDFs corresponding to simulations with varying maximum wall velocities. It is crucial to highlight that in the RDF of the initial position, the first peak is observed at 4 Ri/Rp, which can be attributed to the specific configuration of our simulation environment. Furthermore, in all simulations, the emergence of the first peak around 2 Ri/Rp signifies the likelihood of encountering two particles in direct contact with each other.

Notably, the magnitude of the first peak exhibits a direct correlation with the maximum wall velocity. That is, as the maximum wall velocity is increased we observe a higher frequency of particle collisions (as evidenced in the collision maps in Figure 5.6). Thus, the probability of finding particles in close proximity increases. At the same time, these higher wall velocities exhibit relatively lower RDFs probabilities between 3 to 10 Ri/Rp for the 3 mm/s and 4 mm/s wall velocities, as compared to those at 2 mm/s and even the initial position.

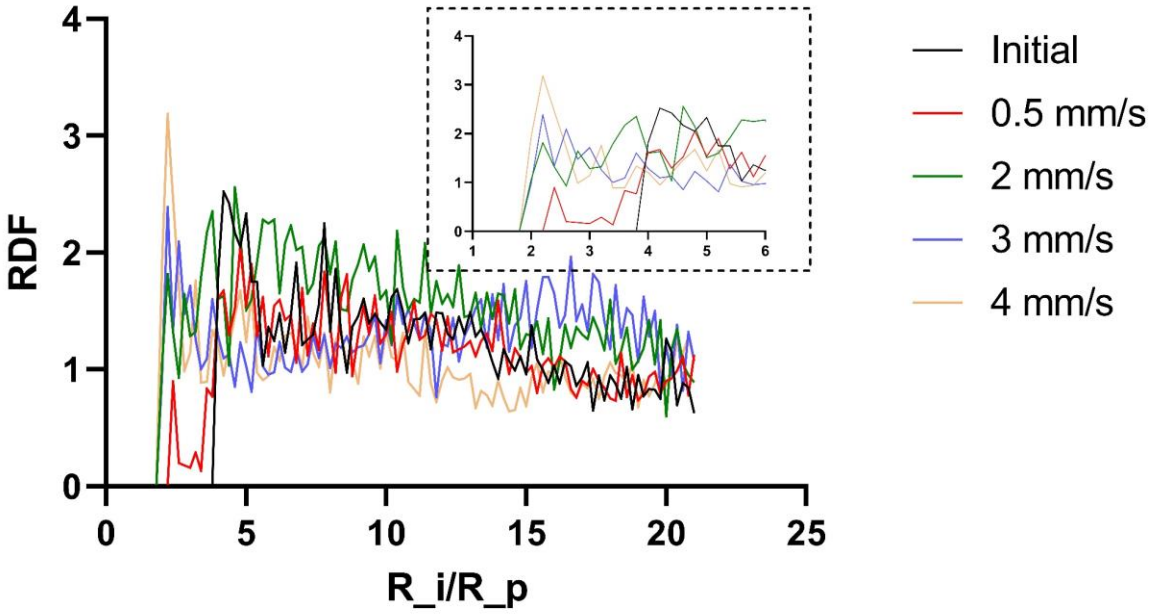

Figure 5.8 RDFs of simulations with different maximum wall velocities. Ri and Rp designate the radii of two distinct entities involved in the analysis. Ri refers to the radius of a spherical shell centered around a reference particle, while Rp represents the radius of the reference particle itself. Ri/Rp value indicated a probability of encountering particles within the spherical shell of radius Ri, centered around the reference particle with radius Rp.

Consider the evolution of the RDFs for the 2 mm/s case, as depicted in Figure 5.9. Under these conditions, we note a pronounced difference between the initial and final stages of the simulation, thereby offering a clear demonstration of RDF curve progression. As a reminder, the initial RDF curve reveals that, for stability purposes, particles are positioned a minimum of two diameters away from each other at the onset of the simulation. As such, there is a strong initial peak in the RDF at a value of 4. As the simulation progresses, we note a decline in the peak observed in the 4 to 5 Ri/Rp range and an increase in the size of the peak between 2 to 4 Ri/Rp. This trend is indicative of particle movement towards each other or a small degree of densification of the suspension.

Intriguingly, while substantial disparities in the RDF curves are evident between the initial position, the 15,000-step, and the 25,000-step marks, the difference between the 25,000-step and the 80,000-step curves is notably smaller. This observation suggests that beyond the 25,000-step point, the system approaches a quasi-steady state, wherein further significant changes in the RDF curves are minimized.

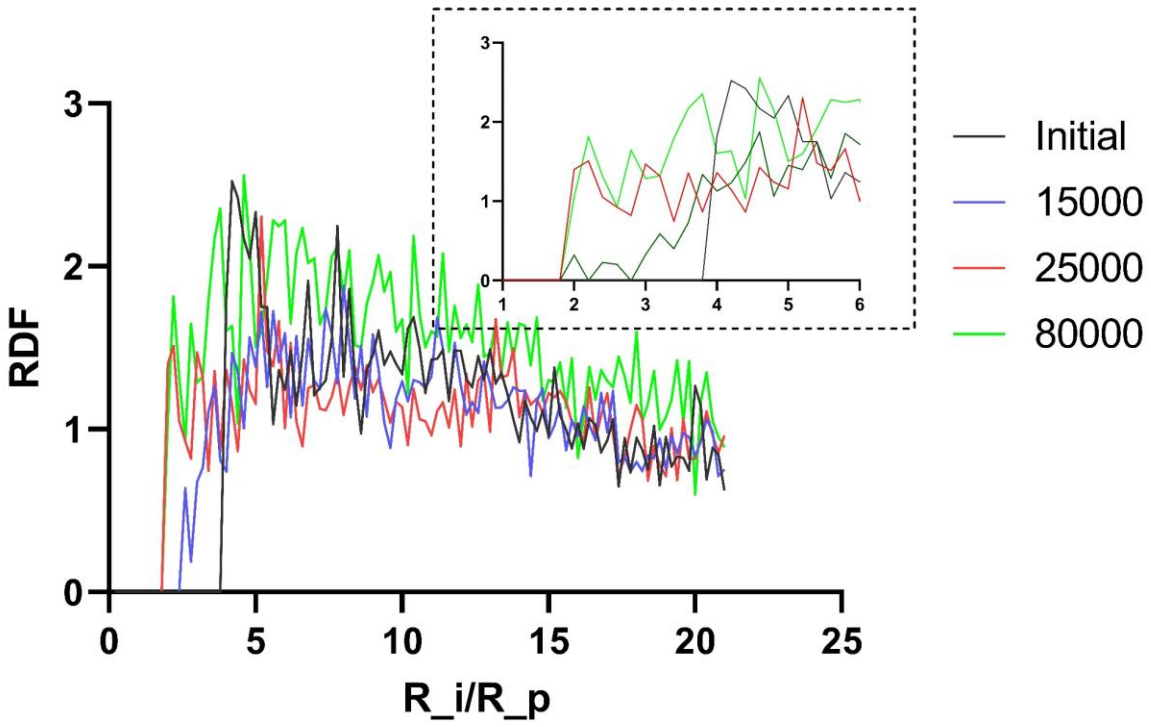

Figure 5.9 The development of the RDFs for the 2 mm/s simulation. While substantial disparities in the RDF curves are evident between the initial position, the 15,000-step, and the 25,000-step marks, the difference between the 25,000-step and the 80,000-step curves is notably smaller.

5.5.3 St Number Analysis

In this section, we examine these results in yet another way. Specifically, here we analyze the Stokes (St) number for both the value based on single-particles (i.e., identifying when a particle is likely to track fluid streamlines) as well as that based on inter-particle interactions (i.e., identifying the degree to which viscous interactions reduce interparticle/collisional inertia) in order to better understand the factors influencing collision frequency and patterns for each experimental setup. First, we calculate the characteristic St number for fluid motion based on single-particles whereby we use the maximum top wall velocity as the characteristic velocity within the flow. In this way, we calculate St values according to Eq(5.1) and show them below in Table 3,

Table 3 Characteristic St numbers

Top wall velocity	0.5 mm/s	2 mm/s	3 mm/s	4 mm/s
Characteristic St number	1.38889	5.55556	8.33333	11.11111

We can see with an increase of the top wall velocity, the one-particle St number increases from near parity to an order of magnitude larger than unity. This indicates that, for most flow conditions examined, we can assume that particles travel across the flow streamlines (which is one mechanism that would allow collisions with other particles). This is consistent with our previous results where it was demonstrated in previous sections, that higher wall velocities result in more frequent collisions. We should note that, even in the case of St values near unity, the finite size of the particles can lead to collisions in regions of the flow with high degrees of shear.

Next, we examine the inter-particle St numbers (i.e., two particle St number) for each pair of particles. The St numbers are calculated based on relative velocities towards each other. As seen

in Figure , we compare the St number distributions of 2,3, and 4 mm/s cases. Each distribution considers the entire simulation time frame (i.e., from the beginning of the simulation to the end). We report the St numbers for any pair of particles whose center-to-center distance is less than or equal to 2 diameters.

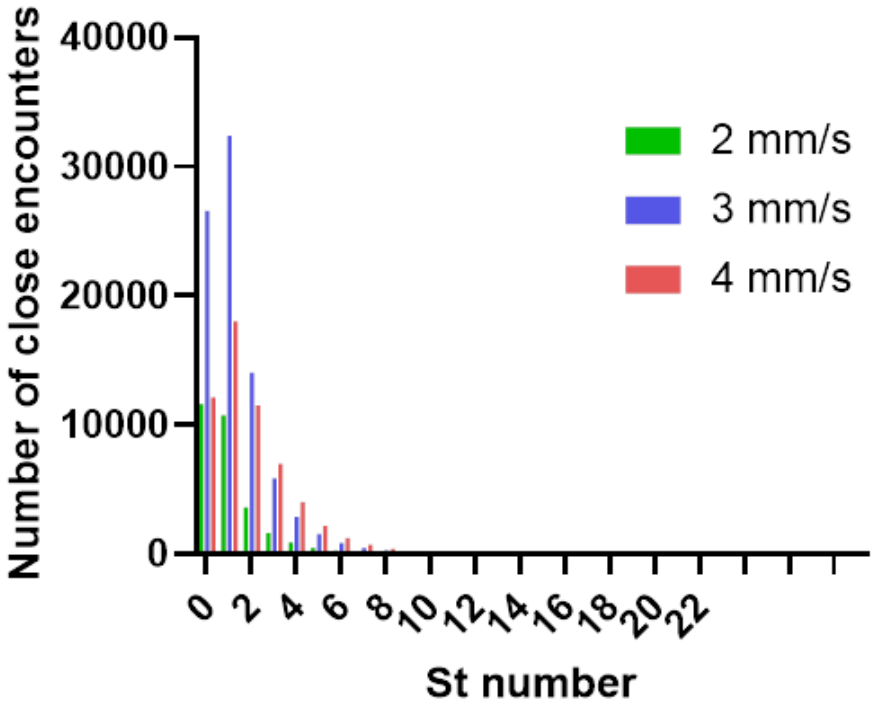

Figure 5.10 St number distributions of 2,3, and 4 mm/s cases. Each distribution considers the entire simulation time frame (i.e., from the beginning of the simulation to the end).

Figure reveals that the 3 mm/s case has the highest number of encounters, implying that among all the cases, 3 mm/s is the most effective in inducing close encounters of particles. The 2 mm/s case has a weaker flow, which is not as sufficient as 3 mm/s, while the 4 mm/s case, with a characteristic one-particle St number of 11.1, has a flow that is strong enough that it results in high values of the two-particle St which can even reach values as high as 50 (resulting in particle

interactions that are more apt to result in rebound). This observation is also supported by the collision map.

Additionally, the St number distribution widens from the 2 mm/s to the 4 mm/s case, indicating a less evenly distributed flow pattern induced by higher top wall velocities, . Interestingly, all cases exhibit a significant number of low St values, while the 3 and 4 mm/s cases have more larger ones. We hypothesize that the causes of the low average collision duration are not only the high inter-particle (two-particle) St number, which leads to the bounce of the two particles after collision, but also the strong and unevenly distributed flow in the system that continually drives the particles away from their close proximity. The St number analysis reveals that the 3 mm/s case is the most effective in inducing close encounters of particles and promoting collision. Future studies may focus on further understanding the interplay between St numbers, flow patterns, and collision dynamics, as well as optimizing the experimental setup to maximize collision efficiency and enhance particle agglomeration processes.

5.6 Conclusion

In this chapter, we utilize the LBM method coupled with the DEM method to simulate particle-particle and particle-liquid interactions in a fluidic environment under different agitation conditions. Our code is validated in a series of situations that can successfully predict particle collision processes. External agitations are induced by introducing an oscillating motion to the top plate. The exploration of various top wall movement patterns, including different frequencies and

amplitudes, reveals the complex relationship between external agitation strength and particle collision dynamics within the fluid. While an increase in maximum wall velocity enhances the system's kinetic energy and momentum, leading to more particle collisions, it also shortens the average duration of these collisions. Moreover, distinct steady states and evolving patterns emerge depending on the chosen maximum wall velocity. A thorough investigation of particle radial distribution functions (RDFs) has been conducted across various simulation scenarios with differing maximum wall velocities. The analysis reveals the impact of wall velocity on the frequency of particle collisions and the formation of agglomerations. The study shows that while increased flow motion induces more particle collisions, it also introduces significant disruption within the system, preventing the formation of larger agglomerations. Furthermore, the 2 mm/s case demonstrates that beyond a certain point in the simulation, a quasi-steady state is reached, resulting in minimized changes in the RDF curves. Finally, the St number analysis reveals that even though the 2 mm/s case drives the most long duration collision process, 3 mm/s is the most effective in inducing close encounters of particles and promoting collision, indicating that somewhere between 2 mm/s and 3 mm/s might provide a better result in terms of both collision duration and frequency. Overall, this comprehensive analysis provides crucial information to support an understanding of the system's behavior under varying conditions and contributes to the broader knowledge of particle interactions and agglomeration dynamics in flow motion simulations.

6.0 Future Studies

The particle-based crystalline materials and their inverted format discussed in this dissertation exhibit great potential in capillary condensation-related applications and beyond. In Chapter 3, the fabrication of closely-packed particle matrix structures with controllable pore sizes demonstrates the possibility of tailoring these materials for various applications. To further advance this research area, a deeper understanding of the underlying physics of particle self-assembly mechanisms, particularly under fluidic environments, will be crucial for driving future discoveries.

Chapter 4 presents a composite material that shows remarkable potential for scavenging ambient water vapor and other condensable vapors through a passive absorption process. This composite, which integrates capturing and storage in a single material, leads to a qualitative change in the absorption behavior, greatly increasing the efficiency of absorption compared to the native material. Future studies could explore the optimization of the composite material by investigating other adsorbent materials, composite structures, and fabrication techniques, enabling the development of new materials with even higher absorption capacities and efficiencies. These materials could be applied across various fields, including water harvesting, air purification, and industrial waste management, contributing to the development of more sustainable and efficient solutions. Moreover, the concept of amplifying native material performance through structural design could inspire the development of new materials for other applications. This fabrication logic could be applied to different adsorbents to enhance the efficiency of the original materials, leading to transformative solutions across a wide range of industries and environmental challenges.

Finally, Chapter 5 investigates the fluid dynamics aspects of particle interactions, providing insights into particle collision dynamics and agglomeration behavior. Future research in this area could explore different fluid properties, external agitation conditions, and material compositions, contributing to a more comprehensive understanding of particle interactions in various fluid environments. This knowledge could be applied to optimize industrial processes involving fluid-particle systems, such as mixing, separation, and chemical reactions.

In conclusion, the findings and future outlooks presented in this dissertation provide a solid foundation for further advancements in the fields of particle self-assembly, porous materials, and fluid dynamics. The potential impact of these advancements is immense, paving the way for innovative and sustainable solutions to pressing global issues. This Chapter lays out a few examples of how we believe this research can be continued to achieve further goals.

6.1 Experiments on Particle Agglomeration in Fluidic Environments under External Agitation Using a Piezo Shaker

The interest in particle agglomeration in fluid domains originated from the ciliary action induced particle clustering in lungs observed by M Lash and M Markovetz. Ciliary action only has an average frequency of 10Hz[169]. After a detailed assessment of the phenomenon, we believe the particle agglomeration is induced by the fluidic motion caused by the low-frequency vibration pattern of the cilia. During our work in Chapter 5.0, we have shown fluidic motion induced particle agglomeration under low-frequency external agitation in our simulation results. To mimic the low frequency and low amplitude vibration, we have also built a shaking device driven by a multilayer

piezoelectric actuator. A multilayer piezoelectric actuator is a ceramic material for converting electrical energy into mechanical energy, such as displacement or force by utilizing the piezoelectric longitudinal effect. It is small in size but can generate high forces and vary frequency from low to high based on the voltage input. The bottom of the piezoelectric actuator was glued with epoxy-based adhesives onto a metal base and the top was pressed with a metal plate with three screw-secured coned-disc springs. The driver device was mounted on the base. Additionally, an accelerometer was mounted on the top metal plate. Figure 6.1 shows the outlook and setup of the shaking device. In order to conduct experiments to validate our simulation results, some modifications are needed to adjust the vibration parameters and pattern of the device.

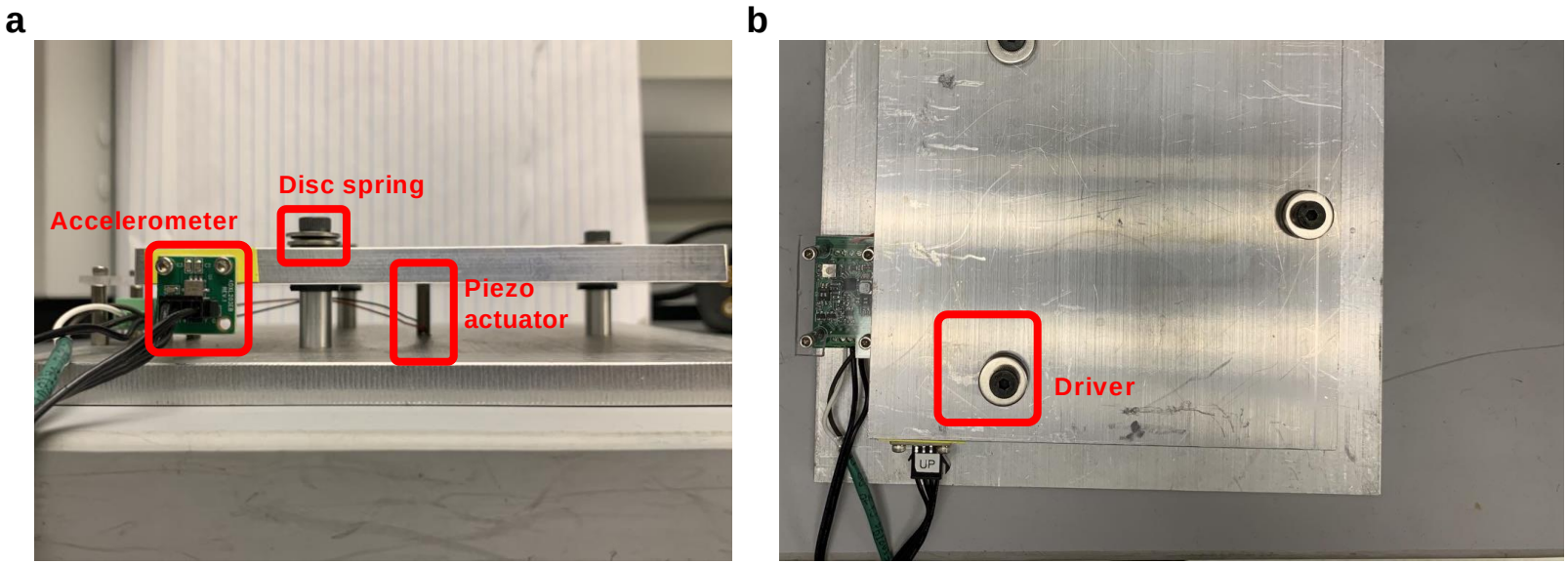

Figure 6.1 a The side view of the piezo shaker. b The top view of the piezo shaker.

6.2 Surface Modifications of the pHEMA Hydrogel

In Chapter 3.0 we have created a multi-layer fine particle crystal on top of the wafer surface. We can create multilayer crystals on pHEMA hydrogel surfaces with a similar idea. However, considering the mechanical stability of the material, the silica particles needed to be "fixed" onto the surface of hydrogel or "connected" to each other. Silane-aided grafting assembly might be considered for further studies. In some preliminary research, we have successfully used 3-aminopropyltrimethoxysilane to functionalize silica particles which, then, were chemically attached to the pHEMA hydrogel surface, as shown in Figure 6.2. The optimization of our methods for the fabrication of nanoparticle multiplayer is the next crucial step for this study.

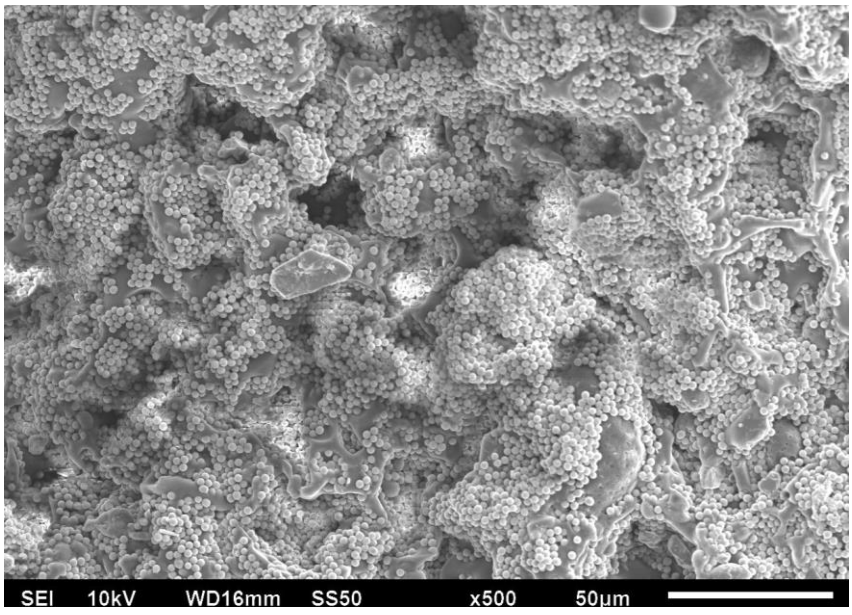

Figure 6.2 SEM picture of silane functionalized silica particles attached on the surface of a pHEMA hydrogel

6.3 Comparison of Our Composite with Other Methods/Materials

To get a better idea of the efficacy of our composite compared to other existing methodologies and materials, we believe an evaluation across different methods/devices would be helpful. As we mentioned previously in Chapter 1.0 and 2.0, there are mainly two types of atmospheric water capturing material/device: saturated water vapor capturing and unsaturated water vapor capturing.

For saturated water vapor capturing, Zhu et al.[170] , inspired by the desert beetle, were able to fabricate PDMS/alginate-based materials via 3D printing. Their material displayed the highest water collection rate of 39.24 L m^{-2} h^{-2}. The lab-scale experiments achieved an average water harvesting capacity[23] of 3 g g^{-1}, which is higher than our hydrogel (1.43 g g^{-1}). However, the strict humidity requirement greatly hinders industrial-scale water production using saturated water vapor capturing techniques. A relatively high cost of the manufacturing process via 3D printing and microfluidic manipulation also needed to be resolved.

On the other hand, the development of unsaturated water vapor capturing is more complicated due to the additional requirements of different driving forces to induce capillary condensation. MOFs have been intensively studied in the past two decades as the representative material of this kind. Among all different MOF materials, MOF-801[90] has shown a water capacity of 0.4 g g^{-1} under 90%RH and 0.28 g g^{-1} under 20%RH, which is the highest water capacity in MOFs to date. While showing a slightly better capacity under 20%RH (around 0.35 g g^{-1}), our composite provides a significant advantage under typical RH ranges (35%-90%RH), showing a capacity of around 1 g g^{-1}.

In the last part of the comparison, we would like to take a look at the energy perspective. A group of researchers[171] has developed a prototype of an unsaturated water vapor-capturing device based on their MOF material. They indicated that, under 20%RH, their device would achieve ~0.1 L m^{-2} water harvesting for 1 hour with low-grade heat at 1 kW m^{-2}. Considering the total duration of solar exposure of 1 hour, their device would harvest 0.1 L m^{-2} of water per 1 kWh m^{-2} energy input. In comparison, our composite can recover ~0.01 g g^{-1} water under 23%RH. Assume the hydrogel density is 1.15 g mL^{-1} and the applied pressure is 10^7 pa. We can briefly calculate the amount of water that would be recovered per 1 kWh energy input,

$$V_{H2O} = \frac{0.01\ g_{H2O} \cdot {g_{gel}}^{-1} \times \rho_{gel}}{\rho_{H2O}} \times V_{gel}$$

$$= \frac{0.01\ g_{H2O} \cdot {g_{gel}}^{-1} \times \rho_{gel}}{\rho_{H2O}} \times \frac{1kWh}{P}$$

$$= \frac{0.01\ g_{H2O} \cdot {g_{gel}}^{-1} \times 1.15g \cdot mL^{-1}}{1g \cdot mL^{-1}} \times \frac{1kWh}{10^7 Pa}$$

$$= 4.14L$$

Thus, for a total of 1 kWh energy input, our composite would have recovered 4.14 L water, although one has to note that it is an estimation of an ideal situation. Because for that to happen in one compression process, we would need a composite/ a group of composites consisting of about 400 kg of hydrogel, or we would need to complete 10^6 cycles on our current composite size. As exciting as seeing our composite outruns MOFs material on purely energy-based analysis, there is still a considerable distance from the ideal situation to realization.

In summary, with respect to absorption capacity, our composite demonstrates superior performance by absorbing 1.25 times more water at 20% RH and 2.5 times more water at higher RH levels under optimal conditions. Concerning energy consumption for water recovery, although

a direct comparison of efficiency is challenging due to differences in the underlying mechanisms, our composite exhibits the potential to recover 40 times more water using the same amount of energy.

Appendix A Stober Method

The Stober method is a sol-gel process to synthesize monodispersed silica particles. In general, silica precursor tetraethyl orthosilicate (Si(OEt)4, TEOS) is hydrolyzed in alcohol, with the presence of ammonia as a catalyst:

$$Si\,(OC_2H_5)_4 + xH_2O \rightarrow Si\,(OC_2H_5)_{4-x}\,(OH)_x + xC_2H_5OH \qquad \textbf{Eq(6.1)}$$

Furthermore, ethoxysilanols and ethanol as products will lead to further hydrolysis of the ethoxy groups and condensation. A vast number of primary particles are nucleated in the precursor solutions and continue growing and forming aggregations. Any new nucleates will be consumed for the growth of large particles. As a result, the synthesized particles in the suspension are highly monodispersed and perfectly spherical.

The size of the particles synthesized can be manipulated by varying the experimental conditions. Any change in the concentration of each ingredient in the precursor (i.e., ammonia, DI water, ethanol, and TEOS) can lead to a different size distribution. In general, the particle size increases with an increase of either TEOS or ammonia concentration in the precursor. We chose to make ammonia excessive, so there will be less residue in the suspension after the reaction, and we controlled the particle size by varying the TEOS concentration. For all synthesis trials, after 12 hours, there is no growth in size, and the size distribution is stabilized.

The size distribution of particles was characterized using a ZetaSizer. A small amount of the sample solution was taken and diluted with ethanol. To ensure the accuracy of the measurement, multiple runs were taken for each sample with various concentrations.

Appendix B Closed-Pack Structure Calculations

Appendix B.1 Face-Centered Cubic

The face-centered cubic contains four atoms per unit cell, as shown in **Error! Reference source not found.**

Appendix Figure 1 The face-centered cubic unit cell

From the structure of FCC, we can see the maximum distance between two particles in a single pore structure is the distance between two particles along the edge of the unit cell cubic. (i.e., AB)

Assume the radius of the particle is,

$$r = a$$

The length of the diagonal on the same side of the unit cell is,

$$4a$$

The length of the side of the unit cell is,

$$\frac{4a}{\sqrt{2}}$$

And the length of the maximum distance is,

$$\frac{4a}{\sqrt{2}} - 2a = 0.8284a$$

Thus, the pore size of the FCC structure is,

$$\frac{0.8284a}{2} = 0.4142a$$

Appendix B.2 Body-Centered Cubic

The body-centered cubic contains two particles in a unit cell, as shown in **Error! Reference source not found.**

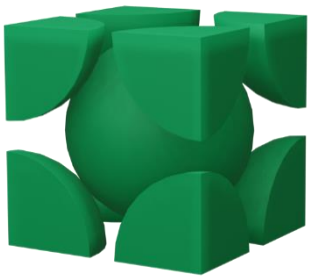

Appendix Figure 2 The body-centered cubic unit cell

The maximum distance between two particles in a single pore structure is no longer along the edge of the cubic like the one in the FCC structure. Instead, in the BCC structure, the four nearest particles form a pyramid structure, as illustrated in **Error! Reference source not found.**

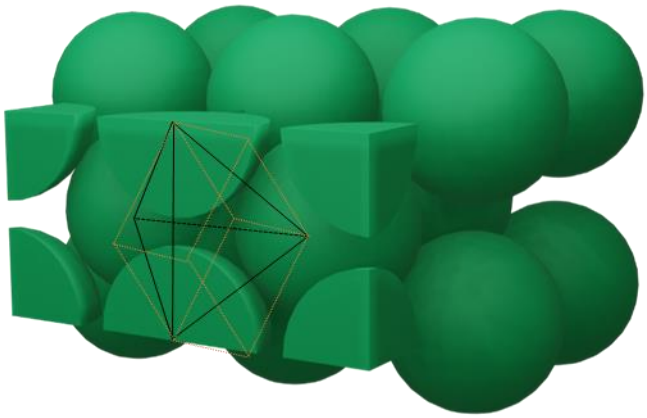

Appendix Figure 3 Pyramid structure formed by four nearest particles in BCC structure

Assume the radius of the particle is,

$$r = a$$

The lengths of the six edges of the pyramid are, respectively, 2a, 2a, 2a, 2a, 2.31a, 2.31a.

Thus, the radius of the sphere that passes all 4 points of the pyramid is,

$$R = \frac{\sqrt{(2a)^2 + \frac{(2.31a)^2}{2}}}{2} = 1.29a$$

So we know the radius of the maximum pore inside the pyramid is,

$$1.29a - a = 0.29a$$

Appendix B.3 Hexagonal Close Packed

In a hexagonal close-packed structure, the third layer has the exact same arrangement of spheres as the first layer and covers all the tetrahedral holes. And the structure repeats itself after every two layers. The structure forming tetrahedral hole is shown in,

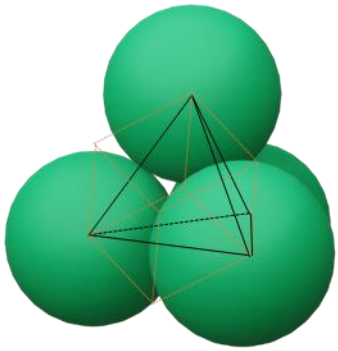

Appendix Figure 4 Tetrahedral hole formed in HCP structure

Assume the radius of the sphere is,

r=a

the length of the face diagonal of the cube is,

2a

And the length of the body diagonal is,

$$\frac{2a}{\sqrt{2}} \times \sqrt{3}$$

Then the radius of the curvature in the void is,

$$\frac{a}{\sqrt{2}} \times \sqrt{3} - a = 0.225a$$

Bibliography

1. Stephen H. Schneider. *Encyclopedia of climate and weather*. *Encyclopedia of climate and weather* (1996). doi:10.5860/choice.49-2412

2. Mozurkewich, M. Mechanisms for the release of halogens from sea-salt particles by free radical reactions. *J. Geophys. Res.* **100**, 14199 (1995).

3. Hanikel, N., Prévot, M. S. & Yaghi, O. M. MOF water harvesters. *Nature Nanotechnology* **15**, 348–355 (2020).

4. Hanikel, N. *et al.* Rapid Cycling and Exceptional Yield in a Metal-Organic Framework Water Harvester. *ACS Cent. Sci.* **5**, 1699–1706 (2019).

5. Parker, A. R. & Lawrence, C. R. Water capture by a desert beetle. *Nature* **414**, 33–34 (2001).

6. Yang, H. *et al.* Temperature-triggered collection and release of water from fogs by a sponge-like cotton fabric. *Adv. Mater.* **25**, 1150–1154 (2013).

7. Jhunjhunwala, S. *et al.* Bioinspired controlled release of CCL22 recruits regulatory T cells in vivo. *Adv. Mater.* **24**, 4735–4738 (2012).

8. Kim, H. *et al.* Water harvesting from air with metal-organic frameworks powered by natural sunlight. **3139**, 1–4 (2017).

9. Kim, H. *et al.* Adsorption-based atmospheric water harvesting device for arid climates. *Nat. Commun.* **9**, 1–8 (2018).

10. Gelb, L. D., Gubbins, K. E., Radhakrishnan, R. & Sliwinska-Bartkowiak, M. Phase separation in confined systems. *Reports Prog. Phys.* **62**, 1573 (1999).

11. Thommes, M. Physical Adsorption Characterization of Nanoporous Materials. (2010). doi:10.1002/cite.201000064

12. Bowden, N., Choi, I. S., Grzybowski, B. a & Whitesides, G. M. Mesoscale self-assembly of hexagonal plates using lateral capillary forces: Synthesis using the ‘capillary bond’. *J. Am. Chem. Soc.* **121**, 5373–5391 (1999).

13. Sattler, K. D. *Handbook of Nanophysics. 1. Principles and Methods*. *Handbook of Nanophysics* **1**, (CRC Press, 2010).

14. Bocquet, L., Charlaix, E., Ciliberto, S. & Crassous, J. Moisture-induced ageing in granular

media and the kinetics of capillary condensation. *Nature* **396**, 735–737 (1998).

15. Honschoten, J. Van, Brunets, N., reviews, N. T.-C. society & 2010, undefined. Capillarity at the nanoscale. *pubs.rsc.org*

16. Malijevský, A., Matter, G. J.-J. of P. C. & 2012, undefined. A perspective on the interfacial properties of nanoscopic liquid drops. *iopscience.iop.org*

17. Barsotti, E., Tan, S. P., Saraji, S., Piri, M. & Chen, J. H. A review on capillary condensation in nanoporous media: Implications for hydrocarbon recovery from tight reservoirs. *Fuel* **184**, 344–361 (2016).

18. UNESCO. *The United Nations World Water Development Report 2018: Nature-Based Solutions for Water. Paris, UNESCO*. *UN Water Report* (2018).

19. Shannon, M. A. *et al.* Science and technology for water purification in the coming decades. *Nature* **452**, 301–310 (2008).

20. Elimelech, M. & Phillip, W. A. The future of seawater desalination: Energy, technology, and the environment. *Science* **333**, 712–717 (2011).

21. Molinari, R., Palmisano, L., Drioli, E. & Schiavello, M. Studies on various reactor configurations for coupling photocatalysis and membrane processes in water purification. *J. Memb. Sci.* **206**, 399–415 (2002).

22. Cambié, D., Bottecchia, C., Straathof, N. J. W., Hessel, V. & Noël, T. Applications of Continuous-Flow Photochemistry in Organic Synthesis, Material Science, and Water Treatment. *Chem. Rev.* **116**, 10276–10341 (2016).

23. Feng, A. *et al.* Recent Development of Atmospheric Water Harvesting Materials: A Review. *ACS Mater. Au* **2**, 576–595 (2022).

24. Horikawa, T., Do, D. D. & Nicholson, D. Capillary condensation of adsorbates in porous materials. *Adv. Colloid Interface Sci.* **169**, 40–58 (2011).

25. Mekonnen, M. M. & Hoekstra, A. Y. Sustainability: Four billion people facing severe water scarcity. *Sci. Adv.* **2**, 1–7 (2016).

26. Hendon, C. H., Rieth, A. J., Korzyński, M. D. & Dincă, M. Grand Challenges and Future Opportunities for Metal-Organic Frameworks. *ACS Cent. Sci.* **3**, 554–563 (2017).

27. Elimelech, M. & Phillip, W. A. The future of seawater desalination: Energy, technology, and the environment. *Science (80-.).* **333**, 712–717 (2011).

28. The Future of Water is up in the Air | XPRIZE. Available at: https://www.xprize.org/prizes/water-abundance/articles/the-future-of-water-is-up-in-the-air. (Accessed: 5th May 2020)

29. Furukawa, H. *et al.* Water adsorption in porous metal-organic frameworks and related materials. *J. Am. Chem. Soc.* **136**, 4369–4381 (2014).

30. Rieth, A. J., Yang, S., Wang, E. N. & Dincă, M. Record Atmospheric Fresh Water Capture and Heat Transfer with a Material Operating at the Water Uptake Reversibility Limit. *ACS Cent. Sci.* **3**, 668–672 (2017).

31. Zhang, L. *et al.* Ultradeep Removal of Moisture in Gases to Parts-per-Billion Levels: The Exploration of Adsorbents. *J. Phys. Chem. C* **122**, 2840–2847 (2018).

32. Hao, G. P. *et al.* Unusual ultra-hydrophilic, porous carbon cuboids for atmospheric-water capture. *Angew. Chemie - Int. Ed.* **54**, 1941–1945 (2015).

33. Klumpen, C., Breunig, M., Homburg, T., Stock, N. & Senker, J. Microporous Organic Polyimides for CO2 and H2O Capture and Separation from CH4 and N2 Mixtures: Interplay between Porosity and Chemical Function. *Chem. Mater.* **28**, 5461–5470 (2016).

34. Meunier, F., Bui, D. T., Chua, K. J. & Gordon, J. M. Comment on "Water harvesting from air with metal-organic frameworks powered by natural sunlight". *Science (80-.).* **358**, eaao0361 (2017).

35. Jin, L., Ma, Y., and, A. J.-S. A. T. C. & 2013, undefined. Investigating the effect of pore proximity on phase behavior and fluid properties in shale formations. *onepetro.org*

36. Travalloni, L., Castier, M., Tavares, F. W. & Sandler, S. I. Thermodynamic modeling of confined fluids using an extension of the generalized van der Waals theory. *Chem. Eng. Sci.* **65**, 3088–3099 (2010).

37. Barsotti, E., Tan, S. P., Saraji, S., Piri, M. & Chen, J. H. A review on capillary condensation in nanoporous media: Implications for hydrocarbon recovery from tight reservoirs. *Fuel* **184**, 344–361 (2016).

38. Charlaix, E. & Ciccotti, M. Capillary Condensation in Confined Media. *Handb. Nanophysics* 219–236 (2009). doi:10.1201/9781420075410-19

39. Honschoten, J. W. V., Brunets, N. & Tas, N. R. Capillarity at the nanoscale. *Chem. Soc. Rev.* **39**, 1096–1114 (2010).

40. Malijevsk, A. & Jackson, G. A perspective on the interfacial properties of nanoscopic liquid drops. *J. Phys. Condens. Matter* **24**, 464121 (2012).

41. Technik, M. T.-C. I. & 2010, undefined. Physical adsorption characterization of nanoporous materials. *Wiley Online Libr.* **82**, 1059–1073 (2010).

42. Golubovic, M., … H. H.-I. J. of & 2006, undefined. Sorption properties for different types of molecular sieve and their influence on optimum dehumidification performance of desiccant wheels. *Elsevier*

43. Yang, H. *et al.* Temperature-Triggered Collection and Release of Water from Fogs by a Sponge-Like Cotton Fabric. *Adv. Mater.* **25**, 1150–1154 (2013).

44. Gur, I., Sawyer, K., Science, R. P.- & 2012, undefined. Searching for a better thermal battery. *science.org* **335**, 1454–1455 (2012).

45. Demir, H., Mobedi, M., Reviews, S. Ü.-R. and S. E. & 2008, undefined. A review on adsorption heat pump: Problems and solutions. *Elsevier*

46. Hepbasli, A., Reviews, Y. K.-R. and S. E. & 2009, undefined. A review of heat pump water heating systems. *Elsevier*

47. Henninger, S., Schmidt, F., engineering, H. H.-A. thermal & 2010, undefined. Water adsorption characteristics of novel materials for heat transformation applications. *Elsevier*

48. Henninger, S. K., Jeremias, F., Kummer, H. & Janiak, C. MOFs for Use in Adsorption Heat Pump Processes. (2012). doi:10.1002/ejic.201101056

49. Yu Gor, G. *et al.* Adsorption of n-pentane on mesoporous silica and adsorbent deformation. *ACS Publ.* **29**, 8601–8608 (2013).

50. Ravikovitch, P., Physicochemical, A. N.-C. and S. A. & 2001, undefined. Characterization of nanoporous materials from adsorption and desorption isotherms. *Elsevier*

51. Pellenq, R. J. M., Coasne, B., Denoyel, R. O. & Coussy, O. Simple phenomenological model for phase transitions in confined Geometry. 2. Capillary condensation/evaporation in cylindrical mesopores. *Langmuir* **25**, 1393–1402 (2009).

52. Gupta, R., Olivier, G. K. & Frechette, J. Invariance of the solid-liquid interfacial energy in electrowetting probed via capillary condensation. *Langmuir* **26**, 11946–11950 (2010).

53. Evans, R., Marini Bettolo Marconi, U. & Tarazona, P. Fluids in narrow pores: Adsorption, capillary condensation, and critical points. *J. Chem. Phys.* **84**, 2376 (1998).

54. Naumov, S., Valiullin, R., Monson, P. A. & Kärger, J. Probing memory effects in confined fluids via diffusion measurements. *Langmuir* **24**, 6429–6432 (2008).

55. Tolman, R. C. The Effect of Droplet Size on Surface Tension. *J. Chem. Phys.* **17**, 333 (2004).

56. Barrett, E. P., Joyner, L. G. & Halenda, P. P. The Determination of Pore Volume and Area Distributions in Porous Substances. I. Computations from Nitrogen Isotherms. *J. Am. Chem. Soc.* **73**, 373–380 (1951).

57. Adolphs, J. Thermodynamics and Modeling of Sorption Isotherms. *Chemie Ing. Tech.* **88**, 274–281 (2016).

58. Horikawa, T., Muguruma, T., Do, D. D., Sotowa, K. I. & Alcántara-Avila, J. R. Scanning curves of water adsorption on graphitized thermal carbon black and ordered mesoporous carbon. *Carbon N. Y.* **95**, 137–143 (2015).

59. Tarazona, P., Marini Bettolo Marconi, U., Evans, R. & Wills, H. H. Phase equilibria of fluid interfaces and confined fluids. *https://doi.org/10.1080/00268978700100381* **60**, 573–595 (2006).

60. Long, Y. *et al.* High pressure effect in nanoporous carbon materials: Effects of pore geometry. *Colloids Surfaces A Physicochem. Eng. Asp.* **437**, 33–41 (2013).

61. Stroud, W. J., Curry, J. E. & Cushman, J. H. Capillary Condensation and Snap-off in Nanoscale Contacts. *Langmuir* **17**, 688–698 (2000).

62. Horikawa, T., Do, D. D. & Nicholson, D. Capillary condensation of adsorbates in porous materials. *Adv. Colloid Interface Sci.* **169**, 40–58 (2011).

63. Quirke, N. (Nick). Adsorption and transport at the nanoscale. 186 (2006).

64. Dyson, P., Ransing, R., Williams, P. H. & Williams, R. *Fluid properties at nano/meso scale: a numerical treatment*. (John Wiley & Sons, 2008).

65. Radhakrishnan, R., Gubbins, K. E. & Sliwinska-Bartkowiak, M. Global phase diagrams for freezing in porous media. *J. Chem. Phys.* **116**, 1147–1155 (2002).

66. Jatukaran, A. *et al.* Direct Visualization of Evaporation in a Two-Dimensional Nanoporous Model for Unconventional Natural Gas. *ACS Appl. Nano Mater.* **1**, 1332–1338 (2018).

67. Shardt, N. & A. W. Elliott, J. Isobaric Vapor–Liquid Phase Diagrams for Multicomponent Systems with Nanoscale Radii of Curvature. *J. Phys. Chem. B* **122**, 2434–2447 (2018).

68. Tsukahara, T., Maeda, T., Hibara, A., Mawatari, K. & Kitamori, T. Direct measurements of the saturated vapor pressure of water confined in extended nanospaces using capillary evaporation phenomena. *RSC Adv.* **2**, 3184–3186 (2012).

69. Yang, Q., Jin, B., Banerjee, D. & Nasrabadi, H. Direct visualization and molecular simulation of dewpoint pressure of a confined fluid in sub-10 nm slit pores. *Fuel* **235**, 1216–1223 (2019).

70. Zandavi, S. H. & Ward, C. A. Nucleation and growth of condensate in nanoporous materials. *Phys. Chem. Chem. Phys.* **17**, 9828–9834 (2015).

71. Zhong, J. *et al.* Capillary Condensation in 8 nm Deep Channels. *J. Phys. Chem. Lett.* **9**, 497–503 (2018).

72. FISHER, L. R. & ISRAELACHVILI, J. N. Direct experimental verification of the Kelvin equation for capillary condensation. *Nature* **277**, 548–549 (1979).

73. Fisher, L. R. & Israelachvili, J. N. Experimental studies on the applicability of the Kelvin equation to highly curved concave menisci. *J. Colloid Interface Sci.* **80**, 528–541 (1981).

74. Kohonen, M. M. & Christenson, H. K. Capillary condensation of water between rinsed mica surfaces. *Langmuir* **16**, 7285–7288 (2000).

75. Kruk, M., Jaroniec, M. & Sayari, A. Application of large pore MCM-41 molecular sieves to improve pore size analysis using nitrogen adsorption measurements. *Langmuir* **13**, 6267–6273 (1997).

76. Lastoskie, C., E. Gubbins, K. & Quirke, N. Pore size distribution analysis of microporous carbons: a density functional theory approach. *J. Phys. Chem.* **97**, 4786–4796 (2002).

77. Miyahara, M., Kanda, H., Yoshioka, T. & Okazaki, M. Modeling capillary condensation in cylindrical nanopores: a molecular dynamics study. *Langmuir* **16**, 4293–4299 (2000).

78. Parsa, E., Yin, X. & Ozkan, E. Direct observation of the impact of nanopore confinement on petroleum gas condensation. in *SPE Annual Technical Conference and Exhibition* (OnePetro, 2015).

79. Factorovich, M. H., Molinero, V., Damián, D. & Scherlis, A. Vapor pressure of water nanodroplets. *ACS Publ.* **136**, 4508–4514 (2014).

80. Kim, S., Kim, D., Kim, J., An, S. & Jhe, W. Direct Evidence for Curvature-Dependent Surface Tension in Capillary Condensation: Kelvin Equation at Molecular Scale. *Phys. Rev. X* **8**, 41046 (2018).

81. Hendon, C. H., Rieth, A. J., Korzyński, M. D. & Dincă, M. Grand Challenges and Future Opportunities for Metal-Organic Frameworks. *ACS Cent. Sci.* **3**, 554–563 (2017).

82. Shannon, M., Bohn, P., Elimelech, M., Nature, J. G.- & 2008, undefined. Science and technology for water purification in the coming decades. *nature.com*

83. Kresge, a C. T., Leonowicz, M. E., Roth, W. J., Vartuli, J. C. & Beck, J. S. Ordered mesoporous molecular sieves synthesized by a liquid-crystal template mechanism. *Nature* **359**, 710–712 (1992).

84. Zhao, D., Huo, Q., Feng, J., Chmelka, B. F. & Stucky, G. D. Nonionic triblock and star diblock copolymer and oligomeric surfactant syntheses of highly ordered, hydrothermally stable, mesoporous silica structures. *J. Am. Chem. Soc.* **120**, 6024–6036 (1998).

85. Nayak, Y. N., Nayak, S., Nadaf, Y. F., Shetty, N. S. & Gaonkar, S. L. Zeolite Catalyzed Friedel-Crafts Reactions: A Review. *Lett. Org. Chem.* **17**, 491–506 (2020).

86. Database of Zeolite Structures. Available at: http://www.iza-structure.org/databases/. (Accessed: 25th March 2023)

87. Prasomsri, T., Jiao, W., Weng, S. Z. & Martinez, J. G. Mesostructured zeolites: bridging the gap between zeolites and MCM-41. *Chem. Commun.* **51**, 8900–8911 (2015).

88. Batten, S. R. *et al.* Terminology of metal–organic frameworks and coordination polymers (IUPAC Recommendations 2013). *Pure Appl. Chem.* **85**, 1715–1724 (2013).

89. Yaghi, O. M. *et al.* Reticular synthesis and the design of new materials. *Nature* **423**, 705–714 (2003).

90. Furukawa, H. *et al.* Water adsorption in porous metal-organic frameworks and related materials. *J. Am. Chem. Soc.* **136**, 4369–4381 (2014).

91. Farha, O. K. *et al.* Metal–organic framework materials with ultrahigh surface areas: is the sky the limit? *J. Am. Chem. Soc.* **134**, 15016–15021 (2012).

92. Canivet, J. *et al.* Structure–property relationships of water adsorption in metal–organic frameworks. *New J. Chem.* **38**, 3102–3111 (2014).

93. Feynman's Talk. Available at: https://www.zyvex.com/nanotech/feynman.html. (Accessed: 26th January 2021)

94. Velev, O. D. & Lenhoff, A. M. Colloidal crystals as templates for porous materials. *Curr. Opin. Colloid Interface Sci.* **5**, 56–63 (2000).

95. Velev, O. D. & Gupta, S. Materials fabricated by micro- and nanoparticle assembly - The challenging path from science to engineering. *Adv. Mater.* **21**, 1897–1905 (2009).

96. Li, F., Josephson, D. P. & Stein, A. Colloids Colloidal Assembly : The Road from Particles to Colloidal Molecules and Crystals Angewandte. 360–388 (2011). doi:10.1002/anie.201001451

97. Park, S. H. & Xia, Y. Assembly of Mesoscale Particles over Large Areas and Its Application in Fabricating Tunable Optical Filters. *Langmuir* **15**, 266–273 (1999).

98. Zhang, Y., Wang, S., Eghtedari, M., Motamedi, M. & Kotov, N. A. Inverted-colloidal-crystal hydrogel matrices as three-dimensional cell scaffolds. *Adv. Funct. Mater.* **15**, 725–731 (2005).

99. Lee, J. I. N. W. O. O., Kim, S. O. Y., Kim, S. S. O. O., Lee, Y. M. O. O. & Lee, K. H. Synthesis and Characteristics of Interpenetrating Polymer Network Hydrogel Composed of Chitosan and Poly (acrylic acid). *Polymer (Guildf).* 113–120 (1998).

100. Ozin, G. A. *et al.* Nanofabrication by self-assembly. *Materials Today* **12**, 12–23 (2009).

101. Anderson, V. J. & Lekkerkerker, H. N. W. Insights into phase transition kinetics from colloid science. *Nature* **416**, 811–815 (2002).

102. Gasser, U. Crystallization in three-and two-dimensional colloidal suspensions. *J. Phys. Condens. Matter* **21**, 203101 (2009).

103. Whitesides, G. M. & Grzybowski, B. Self-assembly at all scales. *Science* **295**, 2418–2421 (2002).

104. Zhu, H. P., Zhou, Z. Y., Yang, R. Y. & Yu, A. B. Discrete particle simulation of particulate systems: A review of major applications and findings. *Chemical Engineering Science* **63**, 5728–5770 (2008).

105. Boncheva, M. & Whitesides, G. M. M aking Things by Self-Assembly. **30**, 736–742 (2005).

106. Zhang, J., Li, Y., Zhang, X. & Yang, B. Colloidal self-assembly meets nanofabrication: From two-dimensional colloidal crystals to nanostructure arrays. *Advanced Materials* **22**, 4249–4269 (2010).

107. Brunauer, S., Emmett, P. H. & Teller, E. Adsorption of gases in multimolecular layers. *J. Am. Chem. Soc.* **60**, 309–319 (1938).

108. De Lange, M. F., Vlugt, T. J. H., Gascon, J. & Kapteijn, F. Adsorptive characterization of porous solids: Error analysis guides the way. *Microporous Mesoporous Mater.* **200**, 199–215 (2014).

109. Van Erp, T. S. & Martens, J. A. A standardization for BET fitting of adsorption isotherms. *Microporous Mesoporous Mater.* **145**, 188–193 (2011).

110. Nourgaliev, R. R., Dinh, T.-N., Theofanous, T. G. & Joseph, D. The lattice Boltzmann equation method: theoretical interpretation, numerics and implications. *Int. J. Multiph. Flow* **29**, 117–169 (2003).

111. Thornton, C. Coefficient of restitution for collinear collisions of elastic-perfectly plastic spheres. (1997).

112. Owen, D. R. J., Leonardi, C. R. & Feng, Y. T. An efficient framework for fluid–structure interaction using the lattice Boltzmann method and immersed moving boundaries. *Int. J. Numer. Methods Eng.* **87**, 66–95 (2011).

113. Lee, J., Laoui, T. & Karnik, R. Nanofluidic transport governed by the liquid/vapour interface. *Nat. Nanotechnol.* **9**, 317–323 (2014).

114. Kim, H. *et al.* Response to Comment on "Water harvesting from air with metal-organic frameworks powered by natural sunlight". *Science (80-.).* **356**, 430–434 (2017).

115. Barsotti, E., Tan, S. P., Saraji, S., Piri, M. & Chen, J. H. A review on capillary condensation in nanoporous media: Implications for hydrocarbon recovery from tight reservoirs. *Fuel* **184**, 344–361 (2016).

116. Park, C. H. *et al.* Nanocrack-regulated self-humidifying membranes. *Nature* **532**, 480–483 (2016).

117. Lee, T., Bocquet, L. & Coasne, B. Activated desorption at heterogeneous interfaces and long-time kinetics of hydrocarbon recovery from nanoporous media. *Nat. Commun.* **7**, 11890 (2016).

118. Wu, K., Chen, Z., Li, X., Guo, C. & Wei, M. A model for multiple transport mechanisms through nanopores of shale gas reservoirs with real gas effect–adsorption-mechanic coupling. *Int. J. Heat Mass Transf.* **93**, 408–426 (2016).

119. Evans, R. & Parry, A. O. Liquids at interfaces: What can a theorist contribute? *J. Phys. Condens. Matter* **2**, 14–32 (1990).

120. Tuller, M., Dani, O. & Dudley, L. M. Adsorption and capillary condensation in porous media: Liquid retention and interfacial configurations in angular pores. *Water Resour. Res.* **35**, 1949–1964 (1999).

121. Yang, Q. *et al.* Capillary condensation under atomic-scale confinement. *ArXiv e-prints* **588**, 1–16 (2020).

122. Klomkliang, N., Do, D. D. & Nicholson, D. Scanning curves in wedge pore with the wide end closed: Effects of temperature. *AIChE J.* **61**, 3936–3943 (2015).

123. Ibrahim, I. a. M., Zikry, a. a. F. & Sharaf, M. a. Preparation of spherical silica nanoparticles: Stober silica. *J. Am. Sci.* **6**, 985–989 (2010).

124. Chen, S.-L., Dong, P. & Yang, G.-H. The size dependence of growth rate of monodisperse silica particles from tetraalkoxysilane. *J. Colloid Interface Sci.* **189**, 268–272 (1997).

125. Min, Y., Akbulut, M., Kristiansen, K., Golan, Y. & Israelachvili, J. The role of interparticle and external forces in nanoparticle assembly. *Nanosci. Technol. A Collect. Rev. from Nat. Journals* 38–49 (2009). doi:10.1142/9789814287005_0005

126. Lash, M. H. *et al.* Non-brownian particle-based materials with microscale and nanoscale hierarchy. *Angew. Chemie - Int. Ed.* **54**, 5854–5858 (2015).

127. Li, R., Shi, Y., Shi, L., Alsaedi, M. & Wang, P. Harvesting Water from Air: Using Anhydrous Salt with Sunlight. *Environ. Sci. Technol.* **52**, 5398–5406 (2018).

128. Zhang, S., Huang, J., Chen, Z. & Lai, Y. Bioinspired special wettability surfaces: from fundamental research to water harvesting applications. *Small* **13**, 1602992 (2017).

129. Metcalfe, G., Shinbrot, T., McCarthy, J. J. & Ottino, J. M. Avalanche mixing of granular solids. *Nature* **374**, 39–41 (1995).

130. Israelachvili, J. N. *Intermolecular and surface forces*. (Academic press, 2011).

131. Hornbaker, D. J., Albert, R., Albert, I., Barabasi, A. L. & Schiffer, P. What keeps sandcastles standing? [4]. *Nature* **387**, 765 (1997).

132. Zhong, J. *et al.* Capillary Condensation in 8 nm Deep Channels. *J. Phys. Chem. Lett.* **9**, 497–503 (2018).

133. Sirghi, L., Szoszkiewicz, R. & Riedo, E. Volume of a nanoscale water bridge. *Langmuir* **22**, 1093–1098 (2006).

134. Baker, J. P., Stephens, D. R., Blanch, H. W. & Prausnitz, J. M. *Swelling Equilibria for Acrylamide-Based Polyampholyte Hydrogels*. *Macromolecules* **25**, (1992).

135. Yu, C., Wang, Y., Lang, X. & Fan, S. A method for seawater desalination via squeezing ionic hydrogels. *Environ. Sci. Technol.* **50**, 13024–13031 (2016).

136. Delavoipière, J. *et al.* Swelling Dynamics of Surface-Attached Hydrogel Thin Films in Vapor Flows. *Langmuir* **34**, 15238–15244 (2018).

137. Liu, Q. & Suo, Z. Osmocapillary phase separation. *Extrem. Mech. Lett.* **7**, 27–33 (2016).

138. Hiemenz, P. C. & Lodge, T. *Polymer chemistry*. (CRC Press, 2007).

139. Treloar, L. R. G. *The physics of rubber elasticity*. (Clarendon Press, 2005).

140. Astin, A. D. Finger force capability: measurement and prediction using anthropometric and myoelectric measures. 1–103 (1999).

141. Lash, M. H., Fedorchak, M. V., McCarthy, J. J. & Little, S. R. Scaling up self-assembly: bottom-up approaches to macroscopic particle organization. *Soft Matter* **11**, 5597–5609 (2015).

142. Nandiyanto, A. B. D., Hagura, N., Iskandar, F. & Okuyama, K. Design of a highly ordered and uniform porous structure with multisized pores in film and particle forms using a template-driven self-assembly technique. *Acta Mater.* **58**, 282–289 (2010).

143. Nandiyanto, A. B. D., Ogi, T., Iskandar, F. & Okuyama, K. Highly ordered porous monolayer generation by dual-speed spin-coating with colloidal templates. *Chem. Eng. J.* **167**, 409–415 (2011).

144. Lotito, V. & Zambelli, T. Approaches to self-assembly of colloidal monolayers: A guide for nanotechnologists. *Adv. Colloid Interface Sci.* **246**, 217–274 (2017).

145. Singh, G., Pillai, S., Arpanaei, A. & Kingshott, P. Layer-by-Layer Growth of Multicomponent Colloidal Crystals Over Large Areas. *Adv. Funct. Mater.* **21**, 2556–2563 (2011).

146. Tan, K. W., Li, G., Koh, Y. K., Yan, Q. & Wong, C. C. Layer-by-layer growth of attractive

binary colloidal particles. *Langmuir* **24**, 9273–9278 (2008).

147. Choi, H. K., Im, S. H. & Park, O. O. Fabrication of unconventional colloidal self-assembled structures. *Langmuir* **26**, 12500–12504 (2010).

148. Kumnorkaew, P. & Gilchrist, J. F. Effect of nanoparticle concentration on the convective deposition of binary suspensions. *Langmuir* **25**, 6070–6075 (2009).

149. Lash, M. H., Fedorchak, M. V., McCarthy, J. J. & Little, S. R. Scaling up self-assembly: bottom-up approaches to macroscopic particle organization. *Soft Matter* **11**, 5597–5609 (2015).

150. Zikanov, O. *Essential computational fluid dynamics*. (John Wiley & Sons, 2019).

151. Kosinski, P. & Hoffmann, A. C. Extended hard-sphere model and collisions of cohesive particles. *Phys. Rev. E - Stat. Nonlinear, Soft Matter Phys.* **84**, 1–13 (2011).

152. Gondret, P., Lance, M. & Petit, L. Bouncing motion of spherical particles in fluids. *Phys. Fluids* **14**, 643–652 (2002).

153. Li, X. Metal assisted chemical etching for high aspect ratio nanostructures: A review of characteristics and applications in photovoltaics. *Curr. Opin. Solid State Mater. Sci.* **16**, 71–81 (2012).

154. Davis, R. H., Serayssol, J.-M. & Hinch, E. J. The elastohydrodynamic collision of two spheres. *J. Fluid Mech.* **163**, 479–497 (1986).

155. Lundberg, J. & Shen, H. H. Collisional restitution dependence on viscosity. *J. Eng. Mech.* **118**, 979–989 (1992).

156. Zhang, J., Fan, L.-S., Zhu, C., Pfeffer, R. & Qi, D. Dynamic behavior of collision of elastic spheres in viscous fluids. *Powder Technol.* **106**, 98–109 (1999).

157. Zenit, R. & Hunt, M. L. Mechanics of immersed particle collisions. (1999).

158. Joseph, G. G., Zenit, R., Hunt, M. L. & Rosenwinkel, A. M. Particle–wall collisions in a viscous fluid. *J. Fluid Mech.* **433**, 329–346 (2001).

159. Donahue, C. M. *et al.* Stokes' cradle: Normal three-body collisions between wetted particles. *J. Fluid Mech.* **650**, 479–504 (2010).

160. Ottino, J. M. *The kinematics of mixing: stretching, chaos, and transport*. (Cambridge Univeristy Press, 1989).

161. Larsen, M. L. & Shaw, R. A. A method for computing the three-dimensional radial distribution function of cloud particles from holographic images. *Atmos. Meas. Tech.* **11**, 4261–4272 (2018).

162. Gavrikov, V. & Stoyan, D. The use of marked point processes in ecological and environmental forest studies. *Environ. Ecol. Stat.* **2**, 331–344 (1995).

163. Martinez, V. J. & Saar, E. *Statistics of the galaxy distribution*. (CRC press, 2001).

164. Lee, K. & Seong, W. Percus–Yevick radial distribution function calculation for a water-saturated granular medium. *Ocean Eng.* **116**, 268–272 (2016).

165. Cherkas, N. L. & Cherkas, S. L. Model of the radial distribution function of pores in a layer of porous aluminum oxide. *Crystallogr. reports* **61**, 285–290 (2016).

166. Erimbetova, L. T., Davletov, A. E., Kudyshev, Z. A. & Mukhametkarimov, Y. S. Influence of polarization phenomena on radial distribution function of dust particles. *Contrib. to Plasma Phys.* **53**, 414–418 (2013).

167. Kopera, B. A. F. & Retsch, M. Computing the 3D Radial Distribution Function from Particle Positions: An Advanced Analytic Approach. *Anal. Chem.* **90**, 13909–13914 (2018).

168. Saw, E.-W., Salazar, J. P. L. C., Collins, L. R. & Shaw, R. A. Spatial clustering of polydisperse inertial particles in turbulence: I. Comparing simulation with theory. *New J. Phys.* **14**, 105030 (2012).

169. Hill, D. B. *et al.* Force generation and dynamics of individual cilia under external loading. *Biophys. J.* **98**, 57–66 (2010).

170. Zhu, P., Chen, R., Zhou, C., Tian, Y. & Wang, L. Asymmetric fibers for efficient fog harvesting. *Chem. Eng. J.* **415**, 128944 (2021).

171. Kim, H. *et al.* Response to Comment on "Water harvesting from air with metal-organic frameworks powered by natural sunlight". *Science (80-.).* **358**, 1–4 (2017).